EUROPEAN ORGANIZATION FOR NUCLEAR RESEARCH

A MEASUREMENT OF SINGLE ELECTRONS, ELECTRON PAIRS, AND ASSOCIATED PHENOMENA, IN PROTON-PROTON COLLISIONS AT THE CERN ISR

F.W. Büsser*), L. Camilleri, L. Di Lella,
B.G. Pope and A.M. Smith
CERN, Geneva, Switzerland

B.J. Blumenfeld and S.N. White**)
Columbia University, New York, USA ***)

A.F. Rothenberg, S.L. Segler and M.J. Tannenbaum
The Rockefeller University, New York, USA +)

M. Banner, J.B. Chèze, H. Kasha++), J.P. Pansart, G. Smadja,
J. Teiger, H. Zaccone and A. Zylberstejn
CEN, Saclay, France

ABSTRACT

Measurements of single electron production in proton-proton collisions at the CERN ISR are presented for five centre-of-mass energies $\sqrt{s}$ = 23.5, 30.6, 44.8, 52.7, and 62.4 GeV. The invariant cross-sections for single electrons with transverse momenta of 0.60 to 4.7 GeV/c are given. Measurements of electron-positron pairs and measurements of charged hadrons produced in association with the single electrons, are also reported.

Geneva - 27 July 1976
(Submitted to Nuclear Physics B)

---

*) Permanent address, II Institut für Experimentalphysik, Hamburg, BRD.
**) Present address, The Rockefeller University, New York, NY, USA.
***) Research supported in part by the NSF.
+) Research supported in part by ERDA.
++) Permanent address, Yale University, New Haven, Conn., USA.

1. INTRODUCTION

The direct production of single electrons and electron pairs in proton-proton interactions has been observed in this experiment performed at the CERN ISR. Some of the results obtained have already been published[1,2]. In this report, the final results are given.

At the time preceding the start of this experiment in 1973, direct production of single electrons had not been observed in hadron collisions[3-5]. The motivation for this study was to search for possible new particles which could be produced at the very high centre-of-mass energy of up to 62.4 GeV available at the ISR. In general, these particles may be too short-lived to be observed directly and can only be identified by detecting their decay products. In this approach, high-energy electrons observed at large angles with respect to the collision axis are selected as a clean signature for the production of these particles. This idea can be traced to the early 1960's, when proton accelerators with laboratory energies of up to 30 GeV became available.

The first opportunity to study weak interactions at high energy was provided by the neutrino beams at the new accelerators[6-8], but it was soon recognized that the intermediate boson $W^{\pm}$, which mediates the weak interactions[9], might be more favourably produced in nucleon-nucleon collisions[10]. The signature of the heavy $W^{\pm}$ would be given by the two-body decay

$$W^{\pm} \rightarrow \ell^{\pm} + \nu \ ,$$

which would create a flux of seemingly direct leptons at large transverse momenta*). It was thought that the transverse momentum spectrum of single leptons from hadron collisions would be composed of the unavoidable, but smoothly falling, background of leptons from the decays of short-lived hadrons, upon which would be superimposed a peak at lepton transverse momentum

$$p_T = \frac{M_W}{2} \ ,$$

where M_W is the mass of the intermediate boson*). This beautiful idea, elegant in its simplicity and qualitativeness, soon became the stimulus of a large body of work[11], both experimental and theoretical.

An objection was raised to the simple idea, when it was realized[12] that the interpretation of such experiments[11], particularly those with null results, would be impossible unless the form factor for the production of the intermediate boson were known. This form factor could be deduced[13] from the measurement of lepton-pair production in hadron collisions; but the existence of such lepton pairs would create additional background in the single lepton spectrum, thus making the detection of a peak more difficult, if not impossible. This new idea established the fundamental relationship between single lepton and lepton-pair experiments, and indicated the importance of doing both types of measurement.

---

*) Isotropic production or decay assumed.

2. APPARATUS

The measurement of single electrons and electron pairs was performed using an apparatus consisting of two spectrometer arms located around 90° on opposite sides of an ISR intersection region (Fig. 1).

Charged particle trajectories in the spectrometers were determined by wire spark chamber planes with magnetostrictive read-out (labelled SC in Fig. 1). Two identical magnets, one for each arm, with gaps of 40 cm vertically by 150 cm horizontally and bending powers of 0.343 T • m, were used to provide a momentum measurement with standard deviation

$$\frac{\Delta p}{p} = \sqrt{(0.025)^2 + (0.02p)^2} \ ,$$

where p is the momentum in GeV/c.

Electron identification was achieved by means of threshold gas Čerenkov counters and electromagnetic shower detectors. In each arm, a gas Čerenkov counter was located in the magnet gap. The Čerenkov counter, $\check{C}_1$, in Arm 1, was filled with isobutane (C_4H_{10}) at atmospheric pressure, and had a pion momentum threshold of 2.8 GeV/c. The Čerenkov counter, $\check{C}_2$, in Arm 2, was filled with air at atmospheric pressure, and had a pion momentum threshold of 5.6 GeV/c. Each Čerenkov counter was segmented into eight independent cells, to provide some spatial resolution; and each cell was equipped with pulse-height measuring electronics.

The electromagnetic shower detector in Arm 1 consisted of a 3 radiation length radiator made up of the lead plates of an optical spark chamber (not triggered in this experiment), followed by a hodoscope of five lead-scintillation sandwich counters (SA), of a total thickness of 2.5 radiation lengths, with pulse-height measurement. The mean pulse height of electrons in this hodoscope was linearly proportional to their energy, having a value of six times the minimum ionization at a laboratory momentum of 1 GeV/c. The r.m.s. energy resolution of the detector was $\Delta E/E = \pm 30\%$. Behind the SA hodoscope was located a lead plate, 5 radiation lengths thick, and a hodoscope H_5 of five scintillation counters.

The electromagnetic shower detector in Arm 2 consisted of an 0.85 radiation-length thick iron plate, followed by a hodoscope of 16 scintillation counters Z, with pulse-height measurement, and then by an array of 119 total absorption lead-glass Čerenkov counters, arranged in 7 horizontal rows of 17 counters each. Each lead-glass counter had a cross-section of 15 × 15 cm^2 and a thickness of 35 cm, corresponding to 14.8 radiation lengths. The r.m.s. energy resolution of this array was measured to be

$$\frac{\Delta E}{E} = 0.017 + \frac{0.064}{\sqrt{E}} \ ,$$

where E is the energy of an electron in GeV. A detailed description of the calibration and monitoring of the lead-glass counters has been published[14].

Each spectrometer arm also contained scintillation counter hodoscopes. Arm 1 had 4 hodoscopes: H_1 of 6 counters 0.5 cm thick × 10 cm wide × 10 cm high, H_2 of 10 counters 0.5 × 10 × 20 cm^3, H_3 of 18 counters 1 × 10 × 65 cm^2 and H_4. Arm 2 had 3 hodoscopes: H_1' of 6 counters 0.5 cm thick × 12.2 cm wide × 12.6 cm high; H_2' of 4 counters 1.0 × 14 × 45 cm^3 and H_3' of 15 counters 1.0 × 20 × 80 cm^3. Hodoscopes H_1 and H_2 in Arm 1, and H_1' in Arm 2, were equipped with pulse-height measuring electronics. More detailed descriptions of the two spectrometers can be found elsewhere[15-17].

Four 1 m^2 scintillation counters, B_1 to B_4, not shown on Fig. 1, were also used. These counters were located downstream of the intersection region, around the vacuum pipes of Ring 1 and Ring 2. For the experiments reported in this publication, these counters were used only to provide triggers for test purposes. Eight additional scintillation counters, collectively denoted as MM, were used to measure and monitor the luminosity of the colliding proton beams, as described in Gresser's Thesis[15].

It should be noted that the centre-of-mass system at the ISR moved away from Arm 1, and towards Arm 2, with a velocity $\beta = 0.1285$. Thus, transverse momenta measured in Arm 1 were approximately 12.1% below their value in the centre-of-mass system, while those measured in Arm 2 were 13.8% above their centre-of-mass value.

3. THE TRIGGERS

The measurements of single electrons and electron pairs proceeded simultaneously. Two types of trigger were used. For each trigger, all the information from both spectrometer arms was recorded on magnetic tape: (i) various scalers including the integrated luminosity monitor; (ii) all spark chamber information; (iii) status bits for all scintillation counters and for each gas Čerenkov cell; (iv) the digitized, integrated pulse heights for each of the H_1, H_2, SA, H_1' and Z counters, as well as for each of the lead-glass blocks and each gas Čerenkov cell.

The principal trigger for both measurements was basically a single electron trigger in Arm 2. This trigger consisted of: (i) a coincidence between the hodoscopes H_1', H_2', H_3', indicating that a charged particle had traversed the spectrometer; (ii) a signal from the gas Čerenkov counter; (iii) an energy deposition in the lead-glass array exceeding a given threshold in any 2 × 2 block area. The threshold of the lead-glass energy requirement was set to one of three nominal values (0.95, 1.16, 1.35 GeV) depending on the ISR luminosity, such that the trigger rate was always less than two per second. It was later determined that these nominal thresholds gave full efficiency for electrons with c.m.s. transverse momenta above 1.6 GeV/c for the highest threshold and 1.3 GeV/c for the lower thresholds.

An independent trigger, based on Arm 1, was also used. This trigger consisted of the coincidence $H_1 \cdot H_2 \cdot H_3 . \check{C}_1 \cdot SA \cdot H_5$. For approximately half of the data taking, the scintillators $H_1' \cdot H_2' \cdot H_3'$ from Arm 2 were also required in coincidence. It should be noted that the counters SA and H_5 were put into the trigger without any requirement on energy deposition; but they nevertheless introduced a triggering bias because low-energy electrons could not penetrate through the 10.5 radiation lengths of lead to give a count in H_5.

The Arm 1 single electron trigger was extremely effective in detecting charged pions with momenta above the $\check{C}_1$ threshold of 2.8 GeV/c. In addition, other triggers, not pertinent to the measurements reported in this publication, were also used. The results of these experiments are reported elsewhere[18,19].

4. ANALYSIS OF THE DATA

The first task of the analysis program was to reconstruct all charged particle trajectories recorded in the spark chambers. Charged particle tracks were required to project to the interaction region, defined as ±25 cm upstream and downstream of the central interaction point and ±2 cm above and below it. Furthermore, charged particle tracks were required to set the bits of all scintillation counters through which their trajectories passed.

The principal backgrounds which could simulate single electron production were (i) electrons from conversions of high transverse momentum photons in the ISR vacuum chamber wall or in the H_1' hodoscope; (ii) electrons from Dalitz decays of high transverse momentum π^0 or η^0 mesons; and (iii) charged hadrons depositing a large fraction of their energy (> 70%) in the lead-glass detector in coincidence with a pulse from the appropriate gas Čerenkov cell.

A selection of single electron events was made by using the following off-line cuts, which were designed to reduce the backgrounds described above, while at the same time maintaining good efficiency for single electrons. The track of interest had to satisfy the following requirements:

i) it had to point to an energy distribution in the lead-glass consistent with that expected for an electron*);

ii) it had to deposit in the lead-glass array a total energy of greater than 1.45 GeV, which corresponds to about 1.3 GeV in the centre-of-mass;

iii) it had to come from the interaction region, and the bits for all of the scintillators and the gas Čerenkov cell through which the track passed had to be set;

iv) its pulse height in H_1' had to be between 0.5 and 1.5 times minimum ionization corresponding to a single particle (this greatly suppressed those electrons due to photon conversions and Dalitz decays);

---

*) These criteria were obtained from studies made using a 3 × 3 block lead-glass array in a high-energy electron beam at the CERN Proton Synchrotron.

v) it had to have a spark in both projections in the first spark chamber, SC1, located before the H_1' hodoscope (this requirement essentially eliminated electrons due to conversions in H_1');

vi) the track momentum as determined by the magnet had to be within ±30% of the energy deposited by the track in the lead-glass array;

vii) its pulse height in the gas Čerenkov cell had to be greater than an empirically determined threshold, which gave optimum separation between electrons and charged hadrons. The last two requirements were applied in order to suppress background due to charged hadrons.

The numbers of events that satisfy all of these cuts are given in Table 1. Measurements were made at five values of centre-of-mass energy $\sqrt{s}$. The integrated luminosities recorded at each energy are also given.

In addition to the sample of single electron events used to measure the inclusive spectrum (Sample E), various subsamples of the data were used to study the following related processes:

i) e^+e^- pairs observed in the same spectrometer (Sample C),
ii) e^+e^- pairs observed in opposite spectrometers (Sample A),
iii) $e^{\pm}$-charged hadron same-side correlations (Sample C),
iv) $e^{\pm}$-charged hadron opposite-side correlations (Sample B).

These subsamples are also given in Table 1. For the analysis of events with more than one charged particle observed in the final state, an additional requirement was made that the particle tracks intersect at a vertex within the interaction region. Also, note that events in which a second track points at the same H_1' counter as the principal track will in general fail the H_1' cut.

Because of the rather loose triggering conditions, apart from the lead-glass energy threshold, it was also possible to relax and change the off-line cuts, so as to obtain other useful data samples. In particular, a sample of selected conversions was obtained simply by changing the H_1' pulse height cut to correspond to two or more charged particles.

Independently of the H_1' cut, a sample of identified e^+e^- pairs with $m_{e^+e^-} < 0.100$ GeV/c^2 was obtained from events in which two overlapping tracks were observed to separate in the magnet (Fig. 2).

Finally, a sample of charged hadrons could be obtained from the tracks that satisfied all the other cuts except Čerenkov pulse height, and did not pass through the Čerenkov cell that had caused the trigger.

It should be noted that an additional requirement, applicable to all the data samples from the Arm 2 trigger, was that all events must have a principal track with momentum of 1.0 GeV/c or greater.

All these various data samples, together with a few special test runs, were used to measure the remaining contributions of background in the sample of single electron events. In addition, the efficiencies of all the cuts could be determined.

5. DETERMINATION OF THE BACKGROUNDS FROM CHARGED HADRONS, PHOTON CONVERSIONS AND DALITZ DECAYS

The backgrounds from charged hadrons, photon conversions, and Dalitz decays, which survive all of the single electron cuts were measured directly by using data taken at $\sqrt{s}$ = 52.7 GeV, for c.m.s. transverse momenta $p_T^* \geq 1.6$ GeV/c. These measurements could be extrapolated to other values of p_T^* and $\sqrt{s}$ by use of the samples of selected conversions and charged hadrons described above.

5.1 Charged hadrons

Figure 3 (curve a) shows the number of single electron candidates satisfying all cuts except the agreement of momentum p, with energy E, as a function of p/E. In order to study the background from charged hadrons, runs were made without requiring the gas Čerenkov counter. The corresponding distribution is shown in Fig. 3 (curve b). In addition, the p/E distribution for pure electrons obtained from the sample of identified e^+e^- pairs is given (curve c).

The distribution of candidates looks very similar to that of the electron sample, except for a definite tail for p/E > 1.3. This tail is due to a small contamination of hadrons. Fitting curve a to a linear combination of curves b and c gives a hadron contribution of (18.6 ± 1.9)% to the accepted events (all cuts applied). In one subsample of the data given in Table 1, the Čerenkov pulse-height cut was not used. The hadron background in this sample was determined in a like manner to be (45 ± 4)%.

It was expected that the hadron background would show a charge asymmetry, because of the possibility that antiprotons could annihilate and thereby deposit an inordinate amount of energy in the lead-glass. Consequently, the charge asymmetry of the hadron background was determined. An asymmetry $a_h = (h^+-h^-)/(h^++h^-) = -(23.7 \pm 3.3)\%$ was found for $p_T^* \geq 1.6$ GeV/c and a value $a_h = -(27.4 \pm 2.6)\%$ for $1.3 \leq p_T^* \leq 1.6$ GeV/c.

5.2 Photon conversions

The background of electrons from photon conversions in the wall of the ISR vacuum chamber was measured by artifically increasing the wall thickness. Under normal running conditions the thickness of the ISR vacuum chamber was equivalent*) to 0.26 mm of stainless steel. Runs were also taken with a 0.50 mm thick stainless steel sheet, or a 0.50 mm thick lead sheet together with a 0.5 cm plastic scintillator, inserted between the vacuum chamber and SC1.

---

*) The true thickness of the vacuum chamber wall was 0.20 mm, but the wall was corrugated, increasing its effective thickness to 0.26 mm.

The yield*) of accepted events is shown in Fig. 4 (curve a) as a function of the number of radiation lengths of material before SC1. The data are normalized to the results obtained under normal running conditions. Also shown (curve b), normalized in the same manner, is the yield*) of photon conversions and Dalitz decays obtained by changing the H_1' pulse-height cut so as to get the selected conversion sample, described above. The ratio of the number of selected conversions to the number of accepted events was 6.2 for normal running conditions.

The very different slopes for these samples clearly demonstrates that only a small fraction of single electron events originate from photon conversions in the ISR vacuum chamber. The slope of the best fit line for the accepted events is proportional to the contribution from this background, which amounts to (8.4 ± 3.1)% of the accepted events. The ratio of the slopes for the two samples is proportional to the rejection of the H_1' cut against electrons from photon conversions, independently of the thickness of the ISR vacuum chamber. The inverse of the rejection factor is found to equal (2.6 ± 1.1)%. These results agree well with the prediction of a Monte Carlo calculation, 8.1% and 2.0%, respectively.

Conversions in the H_1' counter could survive all the cuts if a random spark in SC1 overlapped the particle trajectory. The contribution from this effect was measured by randomly sampling an image region about the centre line of the chamber, and was found to be (0.7 ± 0.2)% of the accepted events.

5.3 Dalitz decay calculation

The rejection for π^0 and η^0 Dalitz decay electrons is expected to be comparable to that obtained for electrons from external conversions of photons from π^0 and $\eta^0 \to \gamma\gamma$ decays. Using the Monte Carlo program mentioned above, the detection efficiency for an electron from Dalitz decay could be calculated by replacing the energy spectrum used to generate conversion pairs from the π^0 and η^0 decay photons, with the doubly differential distribution of pair masses and pair decay angles for Dalitz decay. The distributions used were the following:

i) For photon conversions, the fully screened energy distribution[20] is

$$f(y) = \frac{9}{7}\left[y^2 + (1 - y)^2 + \frac{2}{3}\, y\, (1 - y)\right],$$

where y is the ratio of the energy of one member of the pair to the total pair energy. As this formula is not correct for the very asymmetric pairs which cause the background, the exact energy-sharing distribution for conversions of 1.0 GeV photons was traced from Fig. 38 of Bethe and Ashkin[20] and used in the Monte Carlo program. Multiple scattering was taken into account using the formulation of Bethe and Ashkin as given by Sternheimer[20], who emphasized the validity of this method for thin converters.

*) Note that the data in Fig. 4 (with dashed error bars) have been corrected for radiation of the electrons in the material preceding the magnet. These corrections are described later on.

ii) For Dalitz decays[21]:

$$\frac{1}{\Gamma_{\gamma\gamma}} \frac{d\Gamma_{ee\gamma}}{dm} = \frac{4\alpha}{3\pi} \frac{1}{m} \left(1 - x\right)^3 \left(1 - \frac{x_n}{x}\right)^{\frac{1}{2}} \left(1 + \frac{x_n}{2x}\right),$$

where m equals the mass of the e^+e^- pair, M is the mass of the π^0 or η^0, m_e is the mass of an electron, $x = m^2/M^2$, x_n is the minimum value of x (when $m = 2\ m_e$), and the maximum value of x is 1.0. The total Dalitz conversion probability is

$$\delta = \frac{\Gamma_{ee\gamma}}{\Gamma_{\gamma\gamma}} = \frac{2\alpha}{3\pi} \left(\ln \frac{M^2}{m_e^2} - \frac{7}{2}\right) = \begin{matrix} 1.19\% \text{ for } \pi^0 \\ 1.62\% \text{ for } \eta^0 \end{matrix} .$$

Also, the decay angular distribution of the Dalitz pair in its rest frame is

$$\frac{3}{8} \frac{\left(1 + \cos^2\theta + \frac{x_n}{x} \sin^2\theta\right)}{\left(1 + \frac{x_n}{2x}\right)}$$

where θ is the polar angle of the Dalitz pair in its rest frame, with respect to the total momentum of the pair.

The result of this calculation was that the detection efficiency (within the cut $H_1' < 1.5$) for an electron from π^0 Dalitz decay was 9.5% compared to 2.8% predicted for an electron from external conversion of a π^0 decay photon. Also, the detection efficiency for an electron from η^0 Dalitz decay was 2.64 times as large as that for π^0 Dalitz decay.

The background was computed from these results by using the measured ratio of selected conversions to accepted events, with some additional corrections for the "self-vetoing" and Landau tail effects in the H_1' cut*). Other information required was the conversion probability in the ISR vacuum chamber (1.2% per photon), the value of the η^0 cross-section at the ISR[18] ($\eta^0/\pi^0 = 0.55 \pm 0.10$), and the branching ratio for the two-photon decay of the η^0 ($B_{\eta\to\gamma\gamma} = 0.38$). The value for η^0/π^0 was measured for $p_T^* \geq 3$ GeV/c; but it was assumed that the η^0/π^0 ratio stays constant at 0.55 all the way down to $p_T^* = 1.6$ GeV/c. By this method, the fraction of the accepted events due to π^0 and η^0 Dalitz decay background was found to be $(20.7 \pm 2.5)\%$.

An alternative method is to use the Monte Carlo calculation to predict the ratio of the background from Dalitz decay to that from external conversions. The predicted ratio of 2.53, together with the measured conversion background of $(8.4 \pm 3.1)\%$ gives a Dalitz decay background of $(21.3 \pm 7.8)\%$ of the accepted

*) These corrections are discussed in detail in the section on detection efficiency. The difference between the raw Monte Carlo result of 2.8%, just given for the detection efficiency (within the cut $H_1' < 1.5$), and the 2.0% given a few paragraphs previously, illustrates the effect of these corrections.

events, in excellent agreement. The π^0 and η^0 Dalitz backgrounds can also be absolutely computed by assuming that the π^0 spectrum is given by the charge-averaged British-Scandinavian fit[22], and is in excellent agreement with the results given above.

A summary of the contribution of backgrounds from charged hadrons, photon conversions, and Dalitz decay, to the sample of single electron events at $\sqrt{s}$ = 52.7 GeV and $p_T^* \geq 1.6$ GeV/c is given in Table 2. The single electron signal is (51.6 ± 4.4)% of the accepted events.

5.4 Checks on the background determination

It was possible to make several additional checks on the background determination by using the various data samples in which e^+e^- pairs were observed. The first check of the background comes from the sample of identified e^+e^- pairs. In this sample (2.5 ± 0.4)% of the events are detected as having a single particle in the H_1' counter ($H_1' < 1.5$). The prediction of the Monte Carlo calculation for the fraction of photon conversions and Dalitz decays, with two complete tracks observed in the detector, which would satisfy the cut $H_1' \leq 1.5$ was 1.95%.

A second check comes by looking at the distribution of e^+e^- pairs actually observed in the Arm 2 spectrometer for events satisfying all of the single electron cuts. In order to increase the number of such events, the p_T^* cut for the single electron candidates was reduced to $p_T^* \geq 1.1$ GeV/c (Sample C, Table 1), which increased the sample of single electron candidates to 2806. The observed e^+e^- mass distribution is given in Table 3. Also given is the distribution of like charged electron pairs, which are assumed to be background. The condition for identifying the second particle as an electron was simply that it be counted in the Čerenkov cell through which it passed. Thus the background is particularly large in the 0.1-0.2 GeV/c^2 bin because both tracks tended to pass through the same $\check{C}_2$ cell. The data show some indication of background from π^0 and η^0 Dalitz decays, which is consistent with the values previously given.

Recall that the single electron sample does not contain events in which a second track passes through the same H_1' counter as the principal track, since these events will fail the $H_1' < 1.5$ cut. For one of the other data samples (Sample A, Table 1), a distribution of e^+e^- pairs observed in the Arm 2 spectrometer was obtained, without any H_1' cuts. The total number of events in this sample was 16,892 of which 3191 would remain if the $H_1' \leq 1.5$ cut were made. It should be noted that (45 ± 4)% of these remaining events would be charged hadron background, since the Čerenkov pulse-height cut was not used for this sample. The distribution of e^+e^- pair masses is shown in Fig. 5 for the data with and without the $H_1' \leq 1.5$ cut. For masses below 80 MeV/c^2, the distribution is biased, because the two tracks in

front of the magnet could fall within the resolution of the spark chambers, so that only a single track would be observed and the reconstructed e^+e^- pair mass would be artificially small. Apart from this effect, the data show nothing unexpected in the e^+e^- mass distribution and give efficiencies for the H_1' cut in agreement with the predictions of the Monte Carlo calculation. It is difficult to learn anything else from this distribution, because it is severely biased by its large hadron contamination, so that the computation of pair masses assuming e^+e^- is incorrect.

5.5 Background computations for all $\sqrt{s}$ and p_T^*

The background of charged hadrons, photon conversions, and Dalitz decays determined directly for the sample of single electron events with $\sqrt{s}$ = 52.7 GeV and $p_T^* \geq 1.6$ GeV/c could be extrapolated to other values of $\sqrt{s}$ and p_T^* by using the samples of charged hadrons and selected conversions.

Recall that the charged hadron sample was selected by relaxing the Čerenkov pulse-height cut and taking the events with the "wrong $\check{C}_2$ cell" struck. Approximately the same number of charged hadron and single electron events (0.96:1) is observed at all values of p_T^* and $\sqrt{s}$. Table 4 gives the ratio of charged hadron events to single electron events as a function of p_T^*, for all values of $\sqrt{s}$. There is no marked p_T^* dependence, except perhaps in the highest p_T^* bin. The effect of the Čerenkov pulse-height cut on the charged hadron sample would be to reduce the hadron to electron ratio in all bins by a factor of four or more.

The frequency of the various Čerenkov cells being struck is such that the background from the correct cell being struck at random for a hadron can explain at most half the observed hadron background for $p_T^* \geq 1.6$ GeV/c. This implies that the rest of the hadron background is not random; but results from a correlated count in the same Čerenkov cell, such as would be produced by a knock-on electron. As the knock-on probability is momentum-dependent, while the random background was observed to be essentially momentum-independent, the p_T^* extrapolation of the hadronic background was calculated for three possibilities: all random, all knock-on, and the observed situation of roughly half random plus half knock-on. The results are given in Table 5. These results were parametrized to give the charged hadron background as a fraction of the accepted events as 0.2885 - 0.1966 p_T^*(GeV/c), for all values of $\sqrt{s}$. A point-to-point error of 12% of the background was assigned for the uncertainty of the p_T^* extrapolation and 13% for the possible $\sqrt{s}$ dependence. An additional over-all error of 10% of the background results from the uncertainty of the charged hadron background determination at $\sqrt{s}$ = 52.7 GeV and $p_T^* > 1.6$ GeV/c.

The background of photon conversions and Dalitz decays was determined individually for each bin of p_T^* and $\sqrt{s}$ by using the measured number of selected conversions and the predictions of the Monte Carlo calculation for the fraction of external conversions, π^0 Dalitz decays, and η^0 Dalitz decays, that are detected as single

electrons. The ratio of the events in the single electron sample to those in the selected conversion sample is given in Table 6 for all values of p_T^* and $\sqrt{s}$. The values of this ratio, integrated over transverse momenta $p_T^* > 1.3$ GeV/c at each c.m.s. energy are also given. The results of the Monte Carlo calculation for the detection efficiencies could be simply parametrized:

i) for conversions: 4.0% and 3.5% in the two lowest p_T^* bins and 2.8% for $p_T^* > 1.2$ GeV/c;

ii) for π^0 Dalitz:

$$0.2148 - 0.06933\ p_T^*\ (\text{GeV/c})$$

for $1.0 \leq p_T^* \leq 1.8$ GeV/c; and 9.0% for $p_T^* > 1.8$ GeV/c;

iii) for η^0 Dalitz: the efficiency was equal to the π^0 Dalitz efficiency plus a constant 0.156, for all values of p_T^* and $\sqrt{s}$;

iv) there was no $\sqrt{s}$ dependence, except at $\sqrt{s}$ = 23.5 GeV where the π^0 and η^0 Dalitz efficiencies increased by a constant 0.013, for all values of p_T^*.

Note that the background will be quoted as a percentage of accepted events, but it should be emphasized that the background is determined independently of the number of accepted events, since only the sample of selected conversions is used.

The background determined at $\sqrt{s}$ = 52.7 GeV is given in Table 7a. The errors on the background are statistical. No error is assigned for the Monte Carlo calculation. It was assumed that the η^0/π^0 ratio stays constant at $\eta^0/\pi^0 = 0.55$ for all $p_T^* > 1.0$ GeV/c, and this assumption gives an η^0 contribution of 34% of the conversion and Dalitz background at $p_T^* = 1.1$ GeV/c, rising to 38% for $p_T^* > 1.6$ GeV/c. However, if the η^0/π^0 ratio is set to zero, the conversion and Dalitz background is decreased by only 18% at $p_T^* = 1.1$ GeV/c and 23% for $p_T^* > 1.6$ GeV/c (Table 7b). This comes about because the background determination, using the measured selected conversions, depends on the η^0/π^0 ratio only to the extent that the η^0 and π^0 Dalitz decay branching ratios and detection efficiencies are different.

6. DETECTION EFFICIENCY

The over-all detection efficiency for electrons that satisfy all the cuts was determined to be (36 ± 4)%, as given in Table 8. The geometrical acceptance of the detector is not included in the detection efficiency, but is discussed separately.

Since each track was required to set the bits of all the scintillation counters through which it passed, tracks would be lost if they passed through the small spaces between the counters in each hodoscope (H_1', H_2', H_3'), or if the counters were inefficient. This effect was measured by taking data with only the counters B_1 to B_4 in the trigger, and observing what fraction of the time a counter registered a hit when a track having a bit set in all the other hodoscopes projected through it.

The bit requirement was applied in the same way as in the actual data analysis. The result was an efficiency of 89% for the requirement that a scintillator bit be set in all three hodoscope planes.

The track-fitting efficiency was computed during the track reconstruction for all the chambers, except SC1, by using the redundancy of planes in each spark-chamber array in front of and behind the magnets. Runs with dead planes were discarded. The efficiency of SC1, which was required to have a spark on the track in both projections, was determined separately by using the sample of charged hadron events. The measured efficiencies were 0.87 ± 0.02 for the SC1 requirement, and 0.982 ± 0.004 for a track in the rest of the Arm 2 spectrometer.

The H_1' requirement results in the loss of efficiency of single electrons for two reasons. First of all, events in which a second track passed through the same H_1' counter as the principal track would, in general, fail the $H_1' \leq 1.5$ cut. This self-vetoing effect was determined from the measured associated multiplicity (0.47 ± 0.02) and angular distribution of tracks in front of the magnet, and found to cause a loss in efficiency of (10 ± 2)%. The second effect was from the Landau tail of the pulse-height spectrum, for a single particle traversing H_1'. The shape of the Landau distribution was measured in a test beam at the CERN PS, and scaled to match the observed single ionization peak in the H_1' counter. The efficiency of the H_1' pulse-height requirement, of between 0.5 and 1.5 times the minimum ionization, was thus determined to be 0.85 ± 0.02.

In principle, the efficiency of the p/E cut for electrons could have been determined from Fig. 3 simply by measuring what fraction of the pure electron sample fell within the cut of $0.7 \leq p/E \leq 1.3$. The shape of the p/E curve for a pure electron sample is determined primarily by the resolutions of the momentum and energy measurements; but there is another factor which cannot be ignored. Electrons can radiate in the material preceding the magnet, and therefore the measured momentum will be lower than the true value. For electrons of laboratory momentum 1 GeV/c or higher, all the Brems-photons will be collected in the energy cluster in the lead-glass array, so that the measured energy will be correct. This implies that the p/E curve should show a radiative tail, which is certainly not evident in Fig. 3*). The radiative tail has been suppressed by the seemingly innocuous cut of rejecting events in which the principal track had laboratory momentum of less than 1.0 GeV/c, even if the measured energy was acceptable. With these complications in mind, the efficiency of the p/E cut for electrons was determined to be 0.867 ± 0.02. For the case of perfect resolution, the fraction of events lost by the cut $p/E \geq 0.7$, due to radiation, is trivially computed to be

---

*) Note that the accepted events within the interval $0.7 \leq p/E \leq 1.3$ do show the expected radiative shift. The observed average value of p/E is $\langle p/E \rangle = 0.986 \pm 0.003$.

$t/X_0 \times \ln(1/0.3)$, which equals 6% for this apparatus. Thus the efficiency of the cut $0.7 \leq p/E \leq 1.3$, due to resolution only, was taken to be 0.92 ± 0.02. The correction for radiation is applied later on.

The detection efficiency of the $\check{C}_2$ Čerenkov counter for electrons was measured in place at the ISR by taking a special run with the $\check{C}_2$ signal removed from the trigger. The discriminator thresholds for setting the Čerenkov bits had been adjusted to be fully efficient for a single photoelectron in the photomultipliers. A sample of identified e^+e^- pairs was selected from this data, in the same way as described above, with the additional restriction that both electrons in the pair pass through the same $\check{C}_2$ cell. The Čerenkov bit efficiency for these events, in which two electrons pass through a cell, was observed to be $(98 \pm 2)\%$, from which the single electron efficiency was deduced to be $(86.5 \pm 8)\%$, where the errors are mainly systematic.

The efficiency of the Čerenkov pulse-height cut for electrons was determined by fits to the p/E shape for single electron candidates with and without this cut. The efficiency of the Čerenkov pulse height for electrons, given that the $\check{C}$ bit was set, was found to be 0.783 ± 0.02. The same result was also obtained by a calculation using the observed $\check{C}_2$ pulse-height spectrum.

For another phase of the experiment, it was also desirable to know the efficiency of the cuts which defined the sample of selected conversions. Recall that these cuts were identical to the single electron cuts, except that the H_1' pulse-height cut was reversed, so as to select events with greater than 1.5 times minimum ionization. Note that the inefficiency of the $H_1' \leq 1.5$ cut for single electrons and charged hadrons feeds these events into the selected conversion sample as background. This amounted to 4.0% of the selected conversion sample. Similarly, the inefficiency of the cut $H_1' \geq 1.5$ to select all photon conversions and Dalitz decays provides the background from these processes to the single electron sample. This has already been discussed in detail in the section on background. Apart from this, all the efficiencies of the cuts are identical for the two samples, except for the combined Čerenkov bit and pulse-height requirement which is a factor of 1.08 ± 0.05 more efficient for the selected conversion sample than for the single electron sample, because the selected conversions have a considerable fraction of events in which an e^+e^- pair both go into the same $\check{C}_2$ cell.

7. COMPUTATION OF CROSS-SECTION AND OTHER CORRECTIONS

The inclusive cross-section for single electron production at the five c.m.s. energies $\sqrt{s}$ = 23.5, 30.6, 44.8, 52.7, and 62.4 GeV was computed using the sample of single electron events given in Table 1. The integrated luminosities are also given. Note that at $\sqrt{s}$ = 52.7 GeV, 62.6% of the integrated luminosity was at high

threshold, with full efficiency for c.m.s. transverse momenta $p_T^* \geq 1.6$ GeV/c. Thus the cross-section for the region $1.3 \leq p_T^* \leq 1.6$ GeV/c, at $\sqrt{s} = 52.7$ GeV/c, could only be computed from the data taken with low threshold, 37.4% of the integrated luminosity.

In order to compute the invariant cross-section

$$E \frac{d^3\sigma}{dp^3} = \frac{d^3\sigma}{p_T^* \, dp_T^* \, dy \, d\phi^*} ,$$

the data were histogrammed in bins of c.m.s. transverse momentum p_T^* and c.m.s. rapidity y. It is important to note that the transverse momentum was computed from the energy, as measured in the lead-glass array, assuming the particles to be electrons.

The geometrical acceptance of the detector had been defined, by a fiducial cut at the entrance of the magnet, such that it was independent of momentum for $p_T^* \geq 1.0$ GeV/c. The effective c.m.s. solid angle was $\Delta\Omega^* = 0.168$ sr, with $\Delta\phi^* = \pm 7.0°$ and $\theta^* = 90° \pm 20.0°$. The c.m.s. rapidity distribution of all the events is shown in Fig. 6. The events follow the shape of the acceptance, which implies that the rapidity distribution of the single electrons*) is flat, out to the effective edge of the acceptance $y = \pm 0.36$. The events in each bin were corrected for the acceptance, and the differential cross-section was averaged over the observed rapidity interval.

In principle, the data must be corrected point by point for the effects of resolution of the lead-glass array and radiation of the electrons in the material preceding the magnet. These effects were computed and are given in Table 9. The effect of resolution is to increase the number of events in a bin by 4% at low p_T^* and by 7% at high p_T^*, while the effect of radiation is to reduce the number of events in a bin by 6%, independently of p_T^* and $\sqrt{s}$. The background from Compton scattering in the ISR vacuum chamber is approximately 1½% at 1.5 GeV/c and falls as $1/p_T^*$. The net result of these three small effects is to cancel to a precision of 1.00 ± 0.01 for all values of p_T^* and $\sqrt{s}$.

An additional background to the single electron spectrum arises from the decay in flight of charged and neutral kaons. The flight path in which K leptonic decays can be detected as single electrons in this experiment is roughly 30 cm from the centre of the intersection region. This value, together with data from the British-Scandinavian (BS) Collaboration[22], on kaon production, has been used to estimate the contributions of kaon decay to the single electron cross-section. This contribution amounted to $(10.8 \pm 8.4) \times 10^{-34}$ cm^2/GeV^2 at $p_T^* = 1.35$ GeV/c

*) Note that the rapidity distribution of the selected conversion events is also flat, out to $y = \pm 0.36$.

and $(4.0 \pm 3.0) \times 10^{-36}$ cm^2/GeV^2 at $p_T^* = 2.5$ GeV/c for $\sqrt{s} = 52.7$ GeV, and was subtracted point by point. The contribution to the electron spectrum from strange baryons was less than 1% of the contribution from kaon decay.

The inclusive cross-section computations for single electrons are illustrated in Table 10. For each value of $\sqrt{s}$, the various backgrounds were subtracted bin by bin from the data with the point-to-point errors given in the table, as previously discussed. There is an additional error of ±10% of the charged hadron background, which is an over-all normalization uncertainty due to the original measurement of this background. This effect causes an over-all normalization uncertainty to the cross-section of ±3%, independently of $\sqrt{s}$ and p_T^*.

8. RESULTS OF SINGLE ELECTRON MEASUREMENTS (ARM 2)

After background subtraction, transverse momentum distributions were obtained for e^+ and e^- separately. The charge asymmetry $(e^+-e^-)/(e^++e^-)$ was computed for the data and found to be equal to 0.009 ± 0.057 for the range $1.6 \leq p_T^* \leq 4.7$ GeV/c, and -0.105 ± 0.058 for $1.3 \leq p_T^* \leq 1.6$ GeV/c. The single electron and positron inclusive cross-sections were thus observed to be charge symmetric to the precision quoted, so that the two distributions were averaged. The resulting charge-averaged invariant cross-sections are given in Table 11 at each $\sqrt{s}$ value. In addition to the statistical errors given, there is an over-all normalization uncertainty of ±5% from the luminosity measurement. Furthermore, a possible systematic error of ±3.0% in the absolute energy calibration results in an over-all, s-independent scale normalization error of roughly ±25%. It should be recalled that additional s-independent normalization errors are: ±3% from the background subtraction, ±11% from the detection efficiency, and ±1% from the other small corrections. The systematic errors are summarized in Table 12a.

The charge-averaged invariant cross-sections for inclusive electron production as a function of $\sqrt{s}$ and p_T^* are plotted in Fig. 7. The electron cross-section is a steeply falling function of p_T^*, while yields at a given p_T^* are seen to increase with centre-of-mass energy $\sqrt{s}$. It is important to stress that the inclusive electron cross-sections presented here are absolute cross-sections which could be further analysed in their own right. However, the $\sqrt{s}$ and p_T^* dependences of the inclusive electron cross-section so strongly resemble those of charged pions that it is more reasonable to carry out the analysis in terms of the ratio of electrons to pions.

Comparison with the charge-averaged pion cross-section in the same p_T^* and $\sqrt{s}$ ranges is made using the data of the BS Collaboration[22]. Interpolation between the pion data points is carried out using the fit obtained by the BS group[22]

$$E\frac{d^3\sigma}{dp^3} = \frac{D\, e^{bp_T^*}}{(p_T^{*2} + m^2)^n} \quad ,$$

where the parameters D, b, m and n have been given separately for each $\sqrt{s}$ value. The solid lines in Fig. 7 are the BS charge-averaged pion cross-sections at each $\sqrt{s}$, multiplied by 10^{-4}. For each p_T^* and $\sqrt{s}$ point, the ratio of the charge-averaged inclusive electron cross-section to the charge-averaged pion cross-section has been determined and is shown in Fig. 8a. Again, only statistical errors are used. The data show a slight tendency to increase with p_T^* by an amount (34 ± 14)% per GeV/c; but are also consistent at each $\sqrt{s}$ with being independent of p_T^*, so that an average was made over p_T^* giving the $\sqrt{s}$ dependence shown by the closed circles in Fig. 9. A hypothesis of $\sqrt{s}$ independence of the ratio of electrons to pions (R) for $p_T^* > 1.3$ GeV/c gives

$$R = (0.93 \pm 0.05) \times 10^{-4}$$

with $\chi^2 = 36$ for 39 degrees of freedom. A straight line fit gives

$$R = \left[(0.27 \pm 0.22) + (0.0144 \pm 0.0047)\sqrt{s}\ (\text{GeV})\right] \times 10^{-4}$$

with $\chi^2 = 27$ for 38 degrees of freedom, while a $\sqrt{s}$ dependence of the form

$$R = \left[(0.63 \pm 0.20)\ \ln \sqrt{s}\ (\text{GeV}) - (1.46 \pm 0.74)\right] \times 10^{-4}$$

has $\chi^2 = 26$ for 38 degrees of freedom. In either case the $\sqrt{s}$ dependence is at the 3 standard deviation level. Note that the systematic error has not been included in this analysis, since the variation of the systematic error with $\sqrt{s}$ is estimated[23] to be less than 2%, which would have negligible effect on the above results.

In the preceding analysis, only transverse momenta above 1.3 GeV/c could be considered. This reflects the trigger threshold that required a deposition of energy in the lead-glass array. Block-to-block gain variations resulted in a slow onset of this threshold, such that full efficiency was only achieved for $p_T^* \geq 1.3$ GeV/c. An alternative approach to the absolute cross-section measurement was obtained by studying the ratio of the single electron spectrum to the selected conversion spectrum also measured in this experiment. A selected conversion detected in this apparatus with a $p_T^* \geq 1$ GeV/c, corresponds to a parent π^0 with only slightly larger mean momentum ($\sim$ 500 MeV/c). This is a consequence of the steeply falling spectrum. Since both the electron and selected conversion data suffer from the threshold effect in an identical manner, it was possible by this method to study the p_T^* dependence of the e/π ratio down to $p_T^* = 1.0$ GeV/c.

A Monte Carlo program, with the shape of the primary spectrum given by the BS distribution[22] as an input, was used to convert the measured ratios of single electrons to selected conversions (Table 6) into the ratio of electrons to neutral pions. This approach has the advantage that normalization differences between the

two experiments are avoided and that all luminosity errors cancel. Most importantly, the effect of the possible systematic error in the absolute energy calibration is greatly reduced, resulting in an over-all, s-independent scale normalization error of only ±3.0%. Furthermore, all of the efficiency corrections become ratios so that they cancel exactly, except, obviously, for the H_1' efficiency. Also, as mentioned previously, the Čerenkov counter efficiency is slightly different for the two cases. The result is that the over-all uncertainty from the efficiency is reduced to ±5.7%. The over-all uncertainty from the background is unchanged for the single electron sample, but an additional over-all fractional error of ±1% is caused by the uncertainty in the selected conversion background. The combined $\sqrt{s}$-independent normalization uncertainty of the e/π ratio, from all of the above contributions is 7.3%, Table 12b.

There is, in principle, an additional error introduced in the calculation of the π^0 spectrum from the selected conversion spectrum, because all sources of photons must be taken into account. For the η^0, it was assumed that the ratio of η^0/π^0 cross-sections remains constant at 0.55 for the values of p_T^* used in this analysis, although measurements of η^0 production at the ISR [18] exist only for $p_T^* > 3.0$ GeV/c. Since the η^0 was found to contribute 21% of the selected conversion events, any reduction of the η^0/π^0 ratio from the above value would cause a proportional decrease in the calculated e/π^0 ratio. This is opposite to the effect of the η^0 on the background, where setting the η^0/π^0 ratio to zero will cause the e/π^0 ratio to increase by 0.28×10^{-4} at $p_T^* = 1.1$, 0.23×10^{-4} at $p_T^* = 1.3$, and 0.18×10^{-4} for $p_T^* > 1.6$ GeV/c. These two effects thus tend to cancel, so that the error from the uncertainty of the η^0/π^0 ratio is not particularly important. The existence of any sources of single photons[24] with $p_T^* > 1.0$ GeV/c would have a disproportionate effect on the conversion spectrum, because the conversions would be produced as a secondary process in contrast to the tertiary process for π^0 and η^0. For instance, a single photon continuum at 10% of the π^0 cross-section would cause the e/π^0 ratio, as deduced above, to be 24% too low in the range $1.0 \leq p_T^* \leq 2.0$ GeV/c. However, a much more serious effect of these photons would be their Dalitz decay[24], which would severely change the background computations. This will be discussed later on.

The charge-averaged ratios $(e^+ + e^-)/2\pi^0$ plotted as a function of p_T^* for the various values of $\sqrt{s}$ are shown in Fig. 8b and Table 13. There is no tendency for these data to change with p_T^* over the range $1.0 \leq p_T^* \leq 3.7$ GeV/c, but the data at each value of $\sqrt{s}$ appear to be systematically higher than those of Fig. 8a. The average values of the e/π^0 ratio at each $\sqrt{s}$ for $p_T^* > 1.3$ GeV/c are shown as the open circles in Fig. 9. On the whole, the e/π^0 data agree very well in shape but are systematically higher than the $e/\pi^{\pm}_{BS}$ data by about (19 ± 5)%. The hypothesis of $\sqrt{s}$ independence for the e/π^0 data gives

$$R = (1.14 \pm 0.06) \times 10^{-4}$$

with $\chi^2 = 35$ for 39 degrees of freedom; while a fit of the form

$$R = \left[(0.61 \pm 0.23)\ \ln \sqrt{s}\ (\text{GeV}) - (1.18 \pm 0.87)\right] \times 10^{-4}$$

has a χ^2 of 28 for 38 degrees of freedom and gives a $\sqrt{s}$ dependence of 2.7 standard deviation significance, in excellent agreement with the other method. It is cautioned that the two methods of estimating the ratio of electrons to pions are not independent in that, in both cases, the same single electron spectra and pion spectral shapes are used. Also, the systematic discrepancy between the ratios obtained via the two methods are well within the stated systematic scale error.

The observations of single-lepton production obtained in this experiment can be compared with measurements at Serpuhkov[25] and Fermilab[26,27]. At Serpukhov ($\sqrt{s} = 12$ GeV), a lepton(muon)-to-pion ratio 2.5×10^{-5} was found, while at Fermilab a ratio of (0.8 to $\sim$ 1) $\times 10^{-4}$ was observed at $\sqrt{s} = 24.5$ GeV. Many subsequent measurements have also been made[28].

According to the original motivation for doing single lepton experiments, the presence of such a copious signal at transverse momenta of greater than 1 GeV/c would have been suggestive of the existence of the intermediate boson, via its decay mode

$$W^{\pm} \rightarrow e^{\pm} + \nu\ .$$

The absence of a peak in either the single electron spectrum or the electron-to-pion ratio could have been rationalized as being due to a dominant decay mode of three or more bodies. Alternatively, the single-electron signal could be taken to indicate the production of e^+e^- pairs: either of low mass, produced with transverse momenta of ≥ 1.0 GeV/c; or of high mass, produced essentially at rest in the c.m. system. In order to track down these possibilities, and to explore other ones, various processes related to the single electron production were also measured in this experiment.

9. STUDIES OF SINGLE ELECTRON-HADRON CORRELATIONS

Although the $\sqrt{s}$ and transverse momentum dependence of the single electron production is quite substantial; it is remarkably similar to that observed for inclusive production of hadrons. This is suggestive of a fundamental relationship between the two processes.

Another very striking property of large transverse momentum hadron production at the ISR is that the two-particle correlation function, expressed as the conditional probability of observing another hadron given that one has been observed, is considerably larger and has a different $\sqrt{s}$ and transverse momentum dependence than the fully inclusive hadron cross-section[18]. If the single electron production were fundamentally related to the hadronic process, one would expect that the

two-particle correlation of an electron and a hadron would also be very similar to the hadron-hadron correlation. On the other hand, if the single elctron were produced as the decay product of a heavy particle, like an intermediate boson, etc., it would be surprising if the two-particle correlation were the same as for inclusive hadron production. This is particularly relevant to the case of opposite-side hadron correlations, where there is very little dependence on $\sqrt{s}$, but considerable dependence on the transverse momentum of the triggering particle[18].

The geometry of the two spectrometer arms made it convenient to consider separately the correlation between a single electron and a charged particle emitted in the same spectrometer (Arm 2), and the correlation between a single electron and a charged particle emitted in opposite spectrometers (Arm 2 and Arm 1, respectively). Since the solid-angle acceptance of the spectrometers was rather small, it was necessary to reduce the p_T^* cut on the single electron events, so as to obtain more data. The triggering bias is essentially irrelevant for the correlation studies, since the correlation function is computed from the ratio of observed electron-hadron events to observed electron events. Data Sample B, Table 1 was used for opposite-side correlation studies and data Sample C, Table 1 for same-side studies. Note that background subtraction was not done for the correlation studies, since the background could not be identified event by event. Thus the correlation function is given for the whole data sample, signal plus background. In this p_T^* range, the single electron signal amounts to roughly 35% of the total, and this dilution factor must be taken into account when considering the results.

The data analysis for events with more than one charged track has already been described. The principal track was identified to be a single electron by all the cuts previously given. The second track was identified to be a hadron simply by requiring it not to set the bit of the Čerenkov cell through which it passed; if it set the bit it was identified as an electron. This produced an unavoidable bias for same-side correlations, because the second track could pass through the same Čerenkov cell as the principal track.

In order to overcome this bias, and any others that might occur, the hadron-hadron correlation was determined by using the sample of selected conversion events. Recall that selected conversions correspond to parent π^0 of slightly larger ($\sim$ 500 MeV/c) average transverse momenta.

The number of charged hadrons, with transverse momenta $p_T^* \geq 0.200$ GeV/c, per steradian per GeV/c associated with large p_T^* electrons, was computed and compared with the number associated with selected conversions. The data were corrected for the detection efficiency and geometrical acceptance of the second track. Note that for the same-side correlation no correction was made for the reduced solid angle which results from the loss of single electron events when the correlated hadron

passes through the same H_1' counter as the principal track. The same- and opposite-side correlation functions are shown in Figs. 10 and 11. There is no discernible difference between the correlations of charged hadrons with hadrons or with single electrons, except perhaps for the lowest bin of the same-side correlations, which is particularly subject to the biases mentioned above.

It was also possible to identify the charged hadrons of momentum below 1 GeV/c, for the opposite-side correlations, by using time-of-flight measurements over the 3 m distance between the H_1 and H_3 hodoscopes in Arm 1. The mass spectrum of the opposite-side charged hadrons is shown in Fig. 12 for the single electron sample, and for the combined samples of selected conversions and charged hadrons (wrong $\check{C}_2$ cell). Defining the mass intervals for π, K, and p as shown in the figure, the number of events were found to be in the ratios of 720:50:53 in association with hadrons, and 67:4:3 in association with electrons. Thus, with the statistics given, there is no difference in the particle composition of the charged hadrons observed opposite to a hadron, or to a single electron.

All of these correlation measurements seem to be consistent with the existence of a fundamental relationship between single electron production and inclusive hadron production, at large transverse momenta; i.e. the single electrons do not seem to be associated with any production dynamics, or the production of any special particles, different from those causing high transverse momentum hadron production. However, in Fig. 11, a strong electron-pair signal is indicated in the bin of opposite-side transverse momentum $1.0 \leq p_T^* \leq 2.0$ GeV/c. Also, in two lower bins, the possibility of a small e^+e^- signal cannot be excluded.

10. PRODUCTION OF e^+e^- PAIRS AND VECTOR MESONS

Before consideration of the high-mass electron positron pairs, observed in opposite spectrometers in this experiment, an exploration was made of the possibility that the single electrons could be explained by low mass e^+e^- pairs, or by the leptonic decays of the vector mesons*), ρ, ω^0, and ϕ^0. One fact tending to argue against the high mass pairs as an explanation of the single electrons was that no peak was observed in either the single electron spectrum or the electron-to-pion ratio, for transverse momenta $p_T^* \geq 1.0$ GeV/c.

10.1 Leptonic decays of vector mesons

The electron-to-pion ratio produced by the leptonic decays of the vector mesons, ρ, ω^0 and ϕ^0, near $p_T^* = 1.6$ GeV/c, can be approximately expressed as

$$\frac{e^+ + e^-}{2\pi^0} = \frac{1.08 \times 10^{-5}\, \sigma_{\rho^0} + 1.90 \times 10^{-5}\, \sigma_{\omega^0} + 8.0 \times 10^{-5}\, \sigma_{\phi^0}}{\sigma_{\pi^0} + 0.40\, \sigma_{\rho^\pm} + 0.075\, \sigma_{\omega^0} + 0.01\, \sigma_{\phi^0}} ,$$

*) This had originally been suggested by Boymond et al.[26].

where the σ are the cross-sections for the various particles at $p_T^* = 1.6$ GeV/c. Note that σ_{π^0} represents the direct π^0 cross-section, excluding π^0 from the vector meson decays. The observed π^0 cross-section from all sources, $\sigma_{\pi^0 all}$, is given by the denominator and shows a considerable effect from the $\pi^{\pm}\pi^0$ decay of the $\rho^{\pm}$. Several conclusions can be drawn from the above equation

i) if $\sigma_{\rho^{\pm}} = \sigma_{\rho^0} = \sigma_{\omega^0} = \sigma_{\phi^0} = \sigma_V$, the observed e/π^0 ratio can be explained by $\sigma_V = 2.3\ \sigma_{\pi^0} = 1.1\ \sigma_{\pi^0 all}$;

ii) if $\sigma_{\rho^{\pm}} = \sigma_{\rho^0} = \sigma_{\omega^0} = 0$, then the observed e/π^0 ratio can be explained by $\sigma_{\phi^0} = 1.5\ \sigma_{\pi^0}$;

iii) if $\sigma_{\phi^0} = 0$ and $\sigma_{\rho^{\pm}} = \sigma_{\rho^0} = \sigma_{\omega^0} = \sigma_{\pi^0}$, then the e/π^0 ratio would be 0.20×10^{-4}, which is less than 1/5 of the observed value.

Thus the ρ and ω^0 mesons cannot explain the single electron signals; but the ϕ^0 meson could, if produced with the above cross-section. Such copious ϕ^0 production could easily be observed via the principal decay mode K^+K^-. Thus, a special run was taken in an attempt to detect the ϕ^0 in this mode.

The trigger for this run was a coincidence $H_1 \cdot H_2 \cdot H_3$ in Arm 1, with the additional requirement that two or more counters be struck in the hodoscope H_3. Data were collected for a few hours, corresponding to an integrated luminosity of 1.6×10^{33} cm^{-2} at $\sqrt{s} = 52.7$ GeV, and a mass distribution was obtained for all oppositely charged pairs observed in the spectrometer, assuming that the particles were K^+K^- (Fig. 13a). A cut was also made that required the total momentum of the K^+K^- pair to be ≥ 1.6 GeV/c. In neither case was a signal observed above background. Multiple scattering and decay in flight were important considerations, so that the number of K^+K^- events expected in the apparatus was predicted using a Monte Carlo calculation, which also assumed a flat rapidity (y) distribution in the range $|y| \leq 0.4$ and a transverse momentum distribution of the ϕ^0 identical to that of the π^0. The K^+K^- mass distribution expected for the case $\sigma_{\phi^0} = 10\ \sigma_{\pi^0}$ is shown in Fig. 13b.

Comparison of Figs. 13a and b leads to the conclusion that

$$\sigma_{\phi^0} \leq 0.4\ \sigma_{\pi^0} \text{ to 90\% confidence,}$$

which constraints the possible ϕ^0 contribution to be less than ½ to ¼ of the observed single electron signal[1]. This limit was subsequently corroborated, and improved, at Fermilab[29], where it was concluded that $\sigma_{\phi^0}/\sigma_{\pi^0} \leq 0.055$-$0.103$ for $2.48 \leq p_T^* \leq 3.33$ GeV/c, at $\sqrt{s} = 23$ GeV.

10.2 Same-side e^+e^- pairs

The distribution of e^+e^- pairs, with the second electron observed in the same spectrometer as the principal electron, was obtained from the same data sample as used in the study of same-side electron-hadron correlations. The second track was

identified as an electron if it set the bit of the Čerenkov cell through which it passed, and as a hadron if it did not set the bit. Actually, the mass distribution of same-side e^+e^- pairs has already been given in connection with the determination of the background to the single electron events (Table 3). Only two e^+e^- pairs were observed with mass $m_{ee} \geq 0.300$ GeV/c^2, for a sample of 2806 single electron candidates (Sample C, Table 1).

Recall that there is an intentional bias in this data, because the two tracks were required to pass through different H_1' counters so that the H_1' pulse height cut could be applied. This is illustrated in Fig. 14 where the probability is shown for an e^+e^- pair to satisfy the $H_1' \leq 1.5$ pulse-height cut, given that one member of the pair satisfies all the other single-electron cuts with $p_T^* > 1.6$ GeV/c (solid curve). Also shown is the acceptance probability when the further restriction is made that the second track be fully reconstructed in the spectrometer (broken curve). The effect of the H_1' cut at low masses is clearly seen. For masses above 0.300 GeV/c^2 the bias produced by the H_1' cut is negligible, but the e^+e^- acceptance is poor because the pair opening angle is larger than the detector aperture.

The r.m.s. mass resolution for same-side e^+e^- pairs was approximately constant at ±7% for masses in the range $0.300 \leq m_{ee} \leq 1.00$ GeV/c^2. Ninety-five per cent confidence level upper limits for the production of a particle of a discrete mass m, at $\sqrt{s} = 52.7$ GeV, were obtained by calculating the cross-section for which four events would have been expected in a 0.100 GeV/c^2 wide bin centred around the particle mass. These are given in Table 14, along with the fraction of the observed single electron yield that would be accounted for by the quoted e^+e^- pair cross-section. Note that the cross-sections given are

$$B \frac{d\sigma}{dy} (p_T^* \geq 1.3) ,$$

where B is the branching ratio of the particle m to e^+e^- pairs; and $(d\sigma/dy)(p_T^* \geq 1.3)$ means that the invariant cross-section has been integrated over azimuth and over all transverse momenta $p_T^* \geq 1.3$ GeV/c. An invariant cross-section of the form $E\, d^3\sigma/dp^3 = e^{-3p_T^*}$, for $p_T^* > 1.3$, gave single electron spectra of the correct shape for all masses considered. For comparison with the cross-sections given in Table 14, the integral of the charge-averaged BS [22] pion cross-section at $\sqrt{s} = 52.7$ GeV is

$$\frac{d\sigma}{dy} (p_T^* \geq 1.3)\Big|_{(\pi^+ + \pi^-/2)} = 2.71 \times 10^{-28} \text{ cm}^2$$

and the integrated single electron cross-section has been given in Table 11.
It is clear that the upper limits given in Table 14 allow the single electron yield to be explained by the production of a particle of mass $m \geq 0.800$ GeV/c^2, which decays into e^+e^- pairs. However, the ρ^0 and ω^0 mesons are excluded, because

their leptonic branching ratios are too small; and the ϕ^0 meson is excluded by the measurements discussed previously. Also, it is obvious that models, in which a combination of particles produces the observed single-electron spectrum, can be concocted so that all the limits given in Table 14 are obeyed.

The upper limits for a mass continuum are essentially identical to those given for a discrete particle, if the cross-section quoted is the integral of the continuum over the 0.100 GeV/c^2 wide bin centred on the stated mass:

$$B \frac{d\sigma}{dy} (p_T^* \geq 1.3 \text{ GeV/c}) = 2\pi B \int_{m-0.05}^{m+0.05} dm \int_{1.3}^{\sqrt{s}/2} p_T^* \, dp_T^* \, \frac{E \, d^4\sigma}{dm \, dp^3} .$$

These limits are slightly model-dependent, but only because the acceptance varies over the width of the bin. The variation of the integrated cross-section limit is only 9% for a variation of the mass dependence of the continuum from m^{-1} to m^{-10}. The limits on the differential cross-section can be obtained by noting that the effective width of the 0.100 GeV/c^2 mass bin is 0.065 GeV/c^2 for an m^{-1} distribution and 0.040 GeV/c^2 for an m^{-10} distribution. It is evident that the most stringent limit on a continuum comes from the lowest mass bin. Thus a steeply falling continuum is excluded as the source of the single electrons, unless a cut-off is imposed for masses below 0.700 GeV/c^2. By contrast, a continuum of the form m^{-1} can satisfy the limit at m = 0.400 GeV/c^2, while the contributions at higher masses add up to account for the entire single electron signal[24].

11. OPPOSITE-SIDE e^+e^- PAIRS

The electron pair signal observed in opposite spectrometers has been shown in Fig. 11. In the two lower bins, the upper limits given correspond to the possibility of one event. The strong signal in the bin $1.0 \leq p_{T_1}^* \leq 2.0$ GeV/c (Arm 1) is due to three e^+e^- events observed for a total of 3439 single electron candidates in Arm 2 with $p_{T_2}^* > 1.0$ GeV/c. In order to obtain more data, the Čerenkov pulse-height cut in Arm 2 was relaxed; and the data for all values of $\sqrt{s}$, where both spectrometer arms had been in operation, were combined. Also, the transverse-momentum cut in Arm 2 was restored to $p_T^* \geq 1.3$ GeV/c, so that the lead-glass array would be fully efficient. This resulted in a sample of 3190 single electron candidates (Sample A, Table 1), for an integrated luminosity of 1.79×10^{36} cm^{-2}, distributed over the four values of c.m.s. energy $\sqrt{s}$ = 30.6, 44.8, 52.7, and 62.4 GeV, in the proportions 16%, 27%, 50% and 7%, respectively.

Since both spectrometer arms were used in the analysis of opposite-side electron pair events, data taken with the independent Arm 1 trigger were combined with the sample obtained above from the Arm 2 trigger. As mentioned previously, the Arm 1 trigger also had a threshold bias for electrons; but it provided a big

advantage for the electron-pair search, because the Arm 2 information could be obtained without any lead-glass threshold bias.

In order to select electron-pair events, the usual charged track criteria were used; and all of the single electron cuts, with the exception of the Čerenkov pulse-height cut, were applied in Arm 2. For Arm 1, the charged particle was required to give a pulse height in H_1 of between 0.5 and 1.5 times minimum ionization, corresponding to a single particle; to set the bit of the Čerenkov cell through which it passed; and to give a pulse in the appropriate SA counter of at least two times minimum ionization. Also, in order to be in the bias free region of the shower detectors in each arm, transverse momentum cuts were applied, according to the trigger. The net effect of all these cuts produced detection efficiencies for electrons within the geometrical apertures of Arm 1 and Arm 2 of 84 ± 4% and 45 ± 5%, respectively; and the corresponding hadron rejections obtained were $> 3 \times 10^3$ and 2.0×10^4. The values of the angular apertures and momentum cuts used are given in Table 15.

After all these machinations, a total of 11 electron-pair events was obtained. It is important to note that in all of these events the two electrons had opposite charges. No e^+e^+ or e^-e^- pairs were found.

Three types of background events could contribute to the eleven e^+e^- pairs observed in the experiment: a single electron candidate in Arm 2 in combination with either (i) a charged hadron or (ii) a Dalitz decay or photon conversion in Arm 1, which are misidentified as electrons, and (iii) a real single electron in Arm 1 in combination with an Arm 2 single electron candidate which is not a real electron.

All three types of background could be directly determined by using the 3190 single electron candidates obtained with the Arm 2 trigger. In twenty-two of these events, a charged particle having a c.m.s. momentum above 1 GeV/c was also detected in Arm 1. These twenty-two particles were identified as thirteen charged hadrons (no $\check{C}_1$ signal, SA signal ignored), and nine electrons*). It is known that the charged hadron rejection in Arm 1 is $> 3 \times 10^3$, and the rejection against Dalitz decays and photon conversions is 4.5×10^4, normalized to charged hadrons. Thus the contributions from backgrounds (i) and (ii) turn out to be $< 4.3 \times 10^{-3}$ and 0.3×10^{-3} events, respectively.

From the background determination previously given, for the case of no Čerenkov pulse-height cut, the Arm 2 single electron candidates are known to consist of 31% directly produced electrons, 45% misidentified charged hadrons, and 24% electrons from photon conversions and Dalitz decays. For Arm 1, it is assumed that the natural particle composition (e/π ratio = 1.2×10^{-4}) would be observed, if it were

*) These nine events, together with two other events obtained with the Arm 1 trigger, comprise the eleven e^+e^- pairs observed in this experiment.

not for the Arm 2 trigger. Thus, the contribution from background (iii) becomes 1.1×10^{-3} events, resulting in an over-all background contribution of $(7.0 \pm 2.0) \times \times 10^{-3}$ events to the eleven e^+e^- pairs observed in this experiment. It must be stressed that all types of background would generate an equal number of same-charge and opposite-charge events, while the observed pairs all have opposite charges. It can thus be concluded that the eleven e^+e^- pairs are genuine and correspond to the occurrence of the reaction:

$$p + p \rightarrow e^+ + e^- + \text{anything}. \qquad (1)$$

The invariant mass of each pair was calculated using the momenta of the particles as measured in the magnetic spectrometers. The distribution of invariant masses of the eleven events is shown in Fig. 15 and the events are listed in Table 16. The e^+e^- invariant mass resolution was determined from the known measuring errors on momenta. The resolution function was found to be Gaussian with a standard deviation of 3.5% over the mass interval from 2.5 to 4.0 GeV/c^2.

The geometrical acceptance of the apparatus for reaction (1) as a function of $M(e^+e^-)$ was estimated by a Monte Carlo calculation. A distribution of the form

$$E\frac{d^3\sigma}{dp^3} = \frac{d^2\sigma}{2\pi p_T^* \, dp_T^* \, dy} = e^{-bp_T^*} \qquad (2)$$

was assumed for reaction (1), where p_T^* is the transverse momentum and y the rapidity of the e^+e^- pair in the centre-of-mass system. The flat rapidity distribution of Eq. (2), within acceptance of the apparatus, is suggested by the data (Fig. 16). The value of the geometrical acceptance depends strongly on $\langle p_T^* \rangle = 2/b$, because events with large p_T^* become non-collinear in azimuth and miss the detector. It was determined from the observed events that $\langle p_T^* \rangle \geq 0.67$ GeV/c to 85% confidence, so that the value $b = 3$ GeV^{-1} was used to compute the acceptance. Finally the decay angular distribution was taken to be isotropic in the rest system of the pair*).

The shape of the apparatus acceptance versus $M(e^+e^-)$ is shown in Fig. 15 for both the Arm 1 and Arm 2 triggers. The Arm 2 trigger was active for the full luminosity of the experiment and the Arm 1 trigger for 90% of the luminosity. Hence, the absence of events observed between 2.20 and 2.90 GeV/c^2 strongly suggests that the nine events clustered around $M(e^+e^-) = 3.1$ GeV/c^2 in Fig. 15 result from the reaction

$$p + p \rightarrow J(3.1) + \text{anything}, \qquad (3)$$
$$\qquad\quad \hookrightarrow e^+ + e^-$$

*) Decay angular distributions of the form $\sin^2\theta$ or $1 + \cos^2\theta$ would change the acceptance by a factor of 1.13 and 0.93, respectively.

where J(3.1) is the narrow particle discovered at BNL [30] and SPEAR [31] while this experiment was in progress. These nine events have a mean mass of 3.075 ± 0.037 GeV/c^2 and a standard deviation of 0.11 GeV/c^2. No firm conclusion can be reached on the origin of the two events at higher invariant mass values, although they are consistent, within the mass resolution, with the e^+e^- decay of the $\Psi'(3.7)$ particle[32]. Another interesting fact is that no events are observed for masses $M_{e^+e^-} \geq 4.0$ GeV/c^2.

Using the acceptance calculations discussed above, it is possible to obtain an estimate of the cross-section for reaction (3) at ISR energies. In this experiment, reaction (3) is only observed in the J rapidity interval between -0.32 and +0.32. The cross-section result is expressed in the form

$$B_{ee} \times \left.\frac{d\sigma}{dy}\right|_{y=0} (p + p \to J + \text{anything}) = (7.5 \pm 2.5) \times 10^{-33} \text{ cm}^2$$

averaged over this interval, where B_{ee} is the branching ratio for the decay mode $J(3.1) \to e^+e^-$. It should be noted that a change from $\langle p_T^* \rangle = 0.67$ to higher values in the acceptance calculation would cause the above cross-section to increase. (See Table 17.)

The value of the cross-section for reaction (3) can be compared with that obtained by BNL-MIT [30,33] by converting their measurements to the form given above. Note that BNL-MIT [33] observe a value of $\langle p_T^* \rangle = 0.79$ GeV/c. Our computations give the result that the BNL-MIT data at $\sqrt{s} = 7.5$ GeV can be expressed in the form $B_{ee} \times d\sigma_J/dy\big|_{y=0} = 1.23 \times 10^{-34}$ cm^2, which is two orders of magnitude lower than the corresponding value observed at ISR energies. A comparison with the CHCIF [34] measurement is more difficult, since the experiments were done in disjoint regions of rapidity.

The CHCIF results were converted to differential cross-sections in their variable*) x by using their quoted x dependence, exp (-10 x). The cross-sections were then transformed to be differential in rapidity y, by using the Jacobian $d\sigma/dy = x\, d\sigma/dx$. As shown in Fig. 17, the two experiments are in good agreement. Also note that the p_T^* distribution quoted by CHCIF corresponds to $\langle p_T^* \rangle = 0.707$. If the rapidity distribution of Fig. 17 is taken seriously, then the differential cross-section $B_{ee} \times d\sigma/dy\big|_{y=0}$ given above can be converted into the total cross-section, $B_{ee} \times \sigma_{tot}$, for reaction (3) by multiplying by a factor of 1.6.

Subsequent experiments[35] are all in good agreement with the above results.

---

*) Note that this is not the Feynman x, but is the ratio of the outgoing momentum of the J(3.1) to the momentum of the incident neutron in the laboratory system.

In comparison to the single electron spectrum observed in this experiment, the electron pair yield is rather small. No electron pairs were observed, other than those in the region of the narrow resonances[30-32]. The acceptance calculation discussed above can be used to predict absolutely the spectrum of single electrons due to the production and decay of the J(3.1), as measured in this experiment. An additional assumption used is that Eq. (2) is flat in rapidity for $y \leq 0.8$*). The result is shown in Fig. 18 along with the observed single electron spectrum at $\sqrt{s}$ = 52.7 GeV. For the two values $\langle p_T^* \rangle$ = 1.5 and 2.0 GeV/c, the transverse momentum distributions are in disagreement with the observed single electron data. The other two values of $\langle p_T^* \rangle$ = 1 and 0.67 GeV/c give shapes in agreement with the single electron data for $p_T^* \geq 1.5$ GeV/c; but the magnitude of the cross-section is too small by a factor of three to six. Furthermore, the predicted drop in the cross-section, for $p_T^* \leq 1.5$ GeV/c, is not observed.

Limits on the cross-section of any particles, produced with similar dynamics to the J(3.1) and which undergo two-body decays to e^+e^- or $e^{\pm}\nu$, can be obtained approximately from Fig. 18 by sliding the $\langle p_T^* \rangle$ = 1 GeV/c curve until its peak is at the appropriate transverse momentum and it fits the single electron data above the peak. The limits thus obtained are given in Fig. 19a. Another limit on the production of electron pairs with mass $M_{ee} \geq 4.0$ GeV/c^2 is obtained from the fact that no e^+e^- pairs of such high mass were observed in this experiment. This implies a 95% confidence upper limit of 1/3 the J(3.1) cross-section (Table 17) for the integral of all electron pair production from mass M_{ee} of 4.0 to 50.8 GeV/c^2 at c.m.s. energy $\sqrt{s}$ = 52.7 GeV. Similarly, a limit on lower mass e^+e^- pairs can be obtained from Fig. 11, which showed no evidence for e^+e^- pair production with $p_{T_2}^* \geq 1.0$ GeV/c in Arm 2 and $p_{T_1}^* < 1.0$ GeV/c in Arm 1. The acceptance can be calculated with the same model used for the J(3.1), but in this case the threshold bias in Arm 2 must be taken into account. The threshold bias was determined by reconstructing the π^0 spectrum from the selected conversion events and comparing this spectrum to the charge-averaged BS pion fit[22], with resulting efficiencies of 38% at p_T^* = 1.05 to 85% at p_T^* = 1.25. The upper limits are shown in Fig. 19b and correspond to the cross-section for which three events would have been observed for a discrete particle of mass M. Note that all the limits for B $d\sigma/dy$ for opposite-side e^+e^- pairs are integrals over all transverse momenta, in contrast to the same-side e^+e^- pair limits (Table 14) which are integrals for transverse momenta $p_T^* \geq 1.3$ GeV/c.

*) Note that a rapidity distribution as illustrated in Fig. 17 would cause fewer single leptons to be produced.

12. SINGLE ELECTRON MEASUREMENTS IN ARM 1

The absence of any drop in either the single electron cross-section, or the e/π ratio as p_T^* is reduced all the way down to 1.0 GeV/c, invites speculation as to what might happen at lower values of transverse momenta. The single electrons might continue to follow the pion shape as it changes from the relatively flat distribution observed at high transverse momenta to the $e^{-6p_T^*}$ dependence characteristic of transverse momenta below 1.0 GeV/c. Alternatively, the single electron inclusive cross-section might rise faster than the pion cross-section; or the single electron cross-section might retain the flatter slope characteristic of high transverse momentum hadrons, at the lower values of transverse momenta, which would imply a continued rise in the inclusive electron cross-section as p_T^* is reduced, but a drop in the e/π ratio. Another possibility is that the inclusive cross-section itself would drop, as in the case of production via a two-body decay.

Since the boundless creativity of the human imagination is often chastened by some good experimental data, it was decided to push the measurements of the single electron spectrum to as low a transverse momentum as possible by using data obtained with the independent Arm 1 trigger.

The Arm 1 trigger for single electrons consisted of the coincidence $H_1 \cdot H_2 \cdot H_3 . \check{C}_1 \cdot SA \cdot H_5$, as previously described (see Fig. 1). The purpose of H_5 was to eliminate triggers from low-energy electrons, but it also introduced a triggering bias for high transverse momentum electrons. This bias was measured as described below.

The analysis for single electrons in Arm 1 closely paralleled that for Arm 2: i) tracks were required to set the bits corresponding to the appropriate $\check{C}$ counter cell and scintillation counters traversed; ii) the pulse heights in the H_1 and H_2 hodoscopes were required to be less than 1.3 and 1.5 times minimum ionization, respectively, corresponding to a single particle. (This greatly suppressed electrons from photon conversions and Dalitz decays); iii) no track was accepted unless it included a spark in either SC1 or SC2, located between H_1 and the ISR vacuum chamber (this requirement essentially eliminated electrons from photon conversions in the scintillation counter H_1); iv) the pulse amplitude in the SA counter, in units of the minimum ionization, was divided by 6.0 p, an empirically determined value for an electron of laboratory momentum p. This normalized SA amplitude was required to be within the limits 0.4 and 1.4; v) the pulse height in the appropriate gas $\check{C}$erenkov counter cell had to be greater than an empirically determined threshold, which gave optimum separation between electrons and charged hadrons. Requirements (iv) and (v) greatly reduced background due to charged hadrons.

The effects of the H_5 triggering bias and of all but one of the cuts were measured by subsidiary runs, in particular an inclusive trigger $H_1 \cdot H_2 \cdot H_3$. Also, as in the Arm 2 analysis, samples of charged hadrons (wrong Čerenkov cell) and selected conversions (H_1 cut reversed, H_2 cut ignored, so as to select two or more particles) were obtained. In addition, a sample of identified pions with momentum greater than 2.8 GeV/c was available, since the Čerenkov threshold was rather low and no energy-deposition threshold had been required in the trigger for SA or H_5.

The track reconstruction efficiency for the Arm 1 spectrometer was determined to be 0.96. The combined efficiency of the H_1 and H_2 cuts for single particles was measured with the sample of identified pions, and found to be equal to 0.73 ± 0.03; the efficiency of the H_1 cut alone was found to be 0.86. The efficiency of the Čerenkov pulse-height requirement for electrons, including the efficiency for setting the Čerenkov bit, was determined by using the Čerenkov pulse-height spectrum measured for identified pions of momentum between 3.7 and 5.7 GeV/c. The corresponding electron spectrum was obtained by normalizing the pion spectrum by the ratio $\left[1 - (p_0/p)^2\right]$, where p_0 is the Čerenkov threshold momentum and p is the particle momentum for pions or electrons. The result was an efficiency for electrons of 0.53 ± 0.04.

The background of charged hadrons in the sample of accepted events satisfying all the cuts was determined by comparing the distributions of normalized SA counter amplitudes as measured for hadrons (wrong Č cell), Fig. 20a, and for electrons (selected conversion), Fig. 20b, with that for the accepted events, Fig. 21. The resulting hadron background was $10 \pm 2\%$ for $p_T^* > 1.0$ GeV/c and $7 \pm 1\%$ for $p_T^* < 1.0$ GeV/c. The efficiency of the normalized SA cut for electrons was determined from the effect of the cut on the selected conversion sample. This efficiency was momentum-dependent, varying from 0.69 at $p_T^* = 0.65$ GeV/c to 0.82 at $p_T^* = 0.95$ GeV/c to 0.94 at $p_T^* = 1.50$ GeV/c.

The H_5 triggering bias was measured by determining what fraction of conversions identified from the inclusive trigger also satisfied the H_5 requirement. The bias was found to be transverse momentum dependent with a value of 0.49 ± 0.02 at $p_T^* = 0.65$ GeV/c, improving to 0.74 ± 0.02 at 1.05 GeV/c. The over-all electron detection efficiency due to all the cuts was $13 \pm 1\%$ at $p_T^* = 0.65$ GeV/c, $25 \pm 2\%$ at $p_T^* = 1.05$ GeV/c, and $36 \pm 2\%$ at $p_T^* = 1.95$ GeV/c.

The only effect that was not measured was the background in the accepted events due to electrons from photon conversions and Dalitz decays. This effect was monitored continuously by the selected conversions, i.e. events that satisfied all the cuts except for the single ionization requirement in H_1, with H_2 ignored. Two processes could feed conversions into the single electron sample. The first was electronic inefficiency, or failure of both H_1 and H_2 to record twice the minimum ionization pulse height. This was easily determined from the number of cases in which

H_1 gave single ionization and H_2 double, or vice-versa, and found to be 1.35%. The second process was geometrical, in which only one electron from a conversion or Dalitz pair hit the H_1 and H_2 counters and the other electron missed the counters. The same Monte Carlo program which had been thoroughly checked for Arm 2 was used to predict this effect for Arm 1. Also, in order to keep the analysis as similar as possible for the two arms, only the H_1 cut was used to determine this background. The result of the Monte Carlo calculation was that the detection efficiency (within the cut $H_1 < 1.3$) for an electron from external conversion of a photon was 10% independent of p_T^* compared to 38% at $p_T^* = 0.65$ GeV/c and 24% at $p_T^* = 1.5$ GeV/c for an electron from π^0 Dalitz decay. The detection efficiencies for an electron from η^0 Dalitz decay were 51% at $p_T^* = 0.65$ GeV/c and 41% at $p_T^* = 1.5$ GeV/c.

The background was computed from these numbers by using the measured ratio of the selected conversions to the sample of events satisfying all the single electron cuts, except that H_2 was ignored. For the case $\eta^0/\pi^0 = 0$, the background from conversions and Dalitz decays amounted to 51% of the accepted events (all cuts) for $p_T^* < 1.0$ GeV/c and 40% for $p_T^* \geq 1.0$ GeV/c. For the case $\eta^0/\pi^0 = 0.55$, the background increases slightly to 58% of the accepted events (all cuts) for $p_T^* < 1.0$ GeV/c and 45% for $p_T^* \geq 1.0$ GeV/c.

In the region of lower p_T^*, the background to the single electron spectrum from the decay in flight of charged and neutral kaons takes on increasing importance. This was calculated, as for Arm 2, and the contribution of K decay to the charge-averaged single electron cross-section was found to equal 1.7×10^{-31} cm^2/GeV^2 at $p_T^* = 0.65$ GeV/c, 1.3×10^{-32} cm^2/GeV^2 at $p_T^* = 0.95$ GeV/c, and 2.5×10^{-34} cm^2/GeV^2 at $p_T^* = 1.5$ GeV/c. The background from Compton scattering in the ISR vacuum chamber is also more severe at the lower values of p_T^*, amounting to 7×10^{-32} cm^2/GeV^2 at $p_T^* = 0.65$ GeV/c and 7.5×10^{-33} cm^2/GeV^2 at $p_T^* = 0.95$ GeV/c, for the charge-averaged single electron cross-section.

The single electron data were binned in transverse momenta and averaged for the two values of $\sqrt{s} = 44.8$ and 52.7 GeV. The background was subtracted, and the data corrected for efficiency, bin by bin. The geometrical acceptance of the Arm 1 spectrometer was $\Delta\Omega^* = 0.068$ sr.

The charge-averaged invariant cross-section of single electrons $(e^+ + e^-)/2$, obtained for integrated luminosities of 1.13×10^{35} cm^{-2} at $\sqrt{s} = 52.7$ GeV and 8.15×10^{34} cm^{-2} at $\sqrt{s} = 44.8$ GeV and averaged for the two values of $\sqrt{s}$, are shown in Fig. 22. Some points from the Arm 2 electron analysis are shown for comparison and are in good agreement. The solid line is the British-Scandinavian fit[22] for $(\pi^+ + \pi^-)/2$, multiplied by 10^{-4}. It is evident that as p_T^* is reduced into the range $0.60 \leq p_T^* \leq 1.0$ GeV/c, the single electron spectrum continues to follow the pion shape.

The charge-averaged ratios $(e^+ + e^-)/(\pi^+ + \pi^-)$, are shown in Fig. 23 averaged for the two values of $\sqrt{s}$ = 52.7 and 44.8 GeV. For the range $0.6 \leq p_T^* \leq 2.0$ GeV/c the data are from Arm 1, and for $1.3 \leq p_T^* \leq 4.7$ GeV/c from Arm 2. The charge-averaged pion cross-sections have been taken from the British-Scandinavian fit[22] for both arms, so as to be consistent. Only statistical errors are shown, since the systematic errors are different for the two data sets. The data are in reasonable agreement and appear to indicate a tendency for the e/π ratio to stay constant or decrease as p_T^* is decreased. Clearly no sharp decrease of the single electron cross-section is observed down to $p_T^* = 0.6$ GeV/c. Unfortunately, the large background of π^0 and η^0 Dalitz and K-leptonic decays is a serious experimental problem at low values of p_T^*. These results are in agreement with other experiments[28] in the same range of p_T^*.

The fact that the e/π ratio is observed to change only very slightly over a p_T^* range corresponding to a cross-section variation of five orders of magnitude is quite remarkable and is again suggestive of a fundamental relationship between single electron production and inclusive pion production in proton-proton collisions.

13. SUMMARY AND CONCLUSIONS

From the measurements made in this experiment, we arrive at the following conclusions:

i) A copious single electron yield is observed in proton-proton collisions at a level of about 10^{-4} of the pion cross-section for $0.6 \leq p_T^* \leq 4.7$ GeV/c.

ii) The transverse momentum and $\sqrt{s}$ dependence of the single electron cross-section is remarkably similar to that observed for hadrons.

iii) For values of $p_T^* \geq 1.3$ GeV/c, a statistically significant dependence of the e/π ratio (R) is observed, which can be parametrized by $R = \left[(0.63 \pm 0.20)\ \ln\sqrt{s}\,(\text{GeV}) - (1.46 \pm 0.74)\right] \times 10^{-4}$ over the range $\sqrt{s}$ = 23.5 to 62.4 GeV.

iv) The e^+ and e^- are produced with equal cross-sections to within the measurement error. The asymmetry $(e^+ - e^-)/(e^+ + e^-)$ was found to equal -0.105 ± 0.058 for $1.3 \leq p_T^* \leq 1.6$ GeV/c and 0.009 ± 0.057 for $1.6 \leq p_T^* \leq 4.7$ GeV/c.

v) The rapidity (y) distribution of the single electrons is consistent with being flat out to the edge of the detector acceptance, $y = \pm 0.36$.

vi) Within the solid angles of the two spectrometers of this experiment the two-body correlations of electrons and charged hadrons are similar to those observed for hadron-hadron correlations. Also, the hadrons produced, in association, opposite to high transverse momentum electrons are similar in composition to those hadrons associated with high-p_T hadron production.

vii) The cross-section for e^+e^- pair production from the reaction

$$p + p \to J(3.1) + \text{anything}$$
$$\hookrightarrow e^+e^-$$

is observed at ISR energies and measured to be equal to

$$B_{ee} \times \left.\frac{d\sigma_J}{dy}\right|_{y=0} = (7.5 \pm 2.5) \times 10^{-33} \text{ cm}^2 \text{ for } \langle p_T^* \rangle = 0.67 \text{ GeV/c}.$$

Also the average transverse momentum for J(3.1) production is constrained to be within the limits $0.67 \leq \langle p_T^* \rangle \leq 1.5$ GeV/c.

viii) The contribution of the production and decay of the J(3.1) is found to be between 1/3 to 1/6 of the observed single electron spectrum for $p_T^* \geq 1.5$ GeV/c, and much below the observed single electron yield for $p_T \leq 1.5$ GeV/c.

ix) No electron pairs are observed in this experiment except for the region of the narrow resonances J(3.1) and $\psi'(3.7)$. A 95% confidence level upper limit of 1/3 the J(3.1) cross-section is obtained for the integral of all electron pair production from mass $M_{(e^+e^-)}$ of 4.0 to 50.8 GeV/c^2, at $\sqrt{s}$ = 52.7 GeV.

x) No evidence for the production of low mass e^+e^- pairs in the range $0.400 \leq m_{ee} \leq 1.00$ GeV/c^2 is observed in this experiment. However, the 95% confidence level upper limits obtained for low mass pair production allow the single electron yield to be explained by a particle of mass $m > 0.800$ GeV/c^2 which decays to e^+e^- pairs, with the exception that the ρ^0 and ω^0 mesons are excluded because their leptonic branching ratios are too small. Also, the limits allow the single electron yield to be explained by a low mass e^+e^- continuum[24] falling as 1/m.

xi) The production of the ϕ^0 meson via the K^+K^- decay mode is not observed, so that an upper limit of ¼ to ½ can be placed on the contribution of the ϕ^0 to the single electron yield.

Thus, the origin of the single electrons is undetermined and, as such, represents a challenge to both experimentalists and theorists.

Acknowledgements

We wish to thank Professors R.L. Cool and L.M. Lederman for their continuous interest and support. Mr. M. Lemoine was invaluable in the setting up and running of the experiment. Miss M.-A. Huber provided great help in the data analysis. We also acknowledge the technical help of Messrs. R. Bouhot, R. Gros and G. Sicher. Drs. J.L. Hamel and A.V. Stirling participated in the early stages of the experiment. Finally we thank the ISR experimental support and operation groups for invaluable help and for the excellent performance of the machine.

REFERENCES

1) F.W. Büsser, L. Camilleri, L. Di Lella, B.G. Pope, A.M. Smith, B.J. Blumenfeld, S.N. White, A.F. Rothenberg, S.L. Segler, M.J. Tannenbaum, M. Banner, J.B. Chèze, H. Kasha, J.P. Pansart, G. Smadja, J. Teiger, H. Zaccone and A. Zylberstejn, Phys. Letters 53B (1974), 212.

2) F.W. Büsser, L. Camilleri, L. Di Lella, B.G. Pope, A.M. Smith, B.J. Blumenfeld, S.N. White, A.F. Rothenberg, S.L. Segler, M.J. Tannenbaum, M. Banner, J.B. Chèze, H. Kasha, J.P. Pansart, G. Smadja, J. Teiger, H. Zaccone and A. Zylberstejn, Phys. Letters 56B (1975), 482.

3) M. Banner, J.L. Hamel, J.P. Pansart, A.V. Stirling, J. Teiger, H. Zaccone, J. Zsembery, G. Bassompierre, M. Croissiaux, J. Gresser, R. Morand, M. Riedinger and M. Schneegans, Phys. Letters 44B (1973), 537.

4) F.W. Büsser, L. Camilleri, L. Di Lella, G. Gladding, A. Placci, B.G. Pope, A.M. Smith, J.K. Yoh, E. Zavattini, B.J. Blumenfeld, L.M. Lederman, R.L. Cool, L. Litt and S.L. Segler, Phys. Letters 48B, (1974), 371, 377; Phys. Letters 46B (1973), 471.

5) For single muon production, see G.B. Bondarenko, V.I. Gridasov, Yu.P. Dobretsov, B.A. Dolgoshein, A.S. Dishkant, V.A. Kanzerov, V.G. Kirilov-Ugryumov, A.V. Kiselev, P.L. Nevskij, Yu.P. Nikitin, S.V. Somov and R.M. Sulyaev, Proc. 16th Internat. Conf. on High-Energy Physics, Chicago-Batavia 1972, (National Accelerator Laboratory, Batavia, Ill., 1973), (Eds. J.D. Jackson and A. Roberts), Vol. 2, p. 329.

6) B. Pontecorvo, Soviet Phys. JETP 37 (1959), 751;
B. Pontecorvo and R.M. Ryndin, Proc. 9th Internat. Conf. on High-Energy Physics, Kiev, 1959 (Academy of Science USSR, Moscow 1960), Vol. 2, p. 233.

7) M. Schwartz, Phys. Rev. Letters 4 (1960), 306.

8) T.D. Lee and C.N. Yang, Phys. Rev. Letters 4 (1960), 307.

9) T.D. Lee and C.N. Yang, Phys. Rev. 119 (1960), 1410.

10) J. Bernstein and G. Feinberg, Phys. Rev. 125 (1962), 1741;
J. Bernstein, Phys. Rev. 129 (1963), 2323;
R. Good, W. Melhop, O. Piccioni and R. Swanson, *in* Proc. 12th Internat. Conf. on High-Energy Physics, Dubna, 1964 (Atomizdat, Moscow, 1966), p. 32; see also footnote by A. Zichichi, p. 35.

11) See for example, R.C. Lamb, R.A. Lundy, T.B. Novey, D.D. Yovanovich, M.L. Good, R. Hartung, M.W. Peters and A. Subramanian, Phys. Rev. Letters 15 (1965), 800.
R. Burns, G. Danby, E. Hyman, L.M. Lederman, W. Lee, J. Rettberg and J. Sunderland, Phys. Rev. Letters 15 (1965), 830.
P.J. Wanderer, R.J. Stefanski, R.K. Adair, C.M. Ankenbrandt, H. Kasha, R.C. Larsen, L.B. Leipuner and L.W. Smith, Phys. Rev. Letters 23 (1969), 729.

12) F. Chilton, A. Saperstein and E. Shrauner, Phys. Rev. 148 (1966), 1380.

13) Y. Yamaguchi, Nuovo Cimento 43 (1966), 193.

14) J.S. Beale, F.W. Büsser, L. Camilleri, L. Di Lella, G. Gladding, A. Placci, B.G. Pope, A.M. Smith, B. Smith, J.K. Yoh, E. Zavattini, B.J. Blumenfeld, L.M. Lederman, R.L. Cool, L. Litt and S.L. Segler, Nuclear Instrum. Methods 117 (1974), 501.

15) J. Gresser, Thesis, CRN/HE 74-10 (Centre de recherches nucléaires de Strasbourg, France, 1974).

16) S.N. White, Thesis (Columbia University, NY, 1975), Nevis report 213, 1976.

17) J.P. Pansart, Thesis, Faculté des Sciences d'Orsay, France, 1976.

18) F.W. Büsser, L. Camilleri, L. Di Lella, B.G. Pope, A.M. Smith, B.J. Blumenfeld, S.N. White, A.F. Rothenberg, S.L. Segler, M.J. Tannenbaum, M. Banner, J.B. Chèze, J.L. Hamel, H. Kasha, J.P. Pansart, G. Smadja, J. Teiger, H. Zaccone and A. Zylberstejn, Phys. Letters 55B (1975) 232; Nuclear Phys. B106 (1976) 1.

19) F.W. Büsser, L. Camilleri, L. Di Lella, B.G. Pope, A.M. Smith, B.J. Blumenfeld, S.N. White, A.F. Rothenberg, S.L. Segler, M.J. Tannenbaum, M. Banner, J.B. Chèze, J.L. Hamel, H. Kasha, J.P. Pansart, G. Smadja, J. Teiger, H. Zaccone and A. Zylberstejn, Phys. Letters 61B (1976) 309.

20) H.A. Bethe and J. Ashkin, *in* Experimental nuclear physics (Wiley, New York, 1953) (Ed. E. Segrè), Vol. 1, p. 166.
R.M. Sternheimer, Methods of experimental physics (Academic Press, New York, 1963) (Eds. L.C.L. Yuan and C.S. Wu), Vol. 5A, Nuclear Physics, p. 1.

21) R.H. Dalitz, Proc. Roy. Soc. A 64 (1951), 667;
N.M. Kroll and W. Wada, Phys. Rev. 98 (1955), 1355.
D.W. Joseph, Nuovo Cimento 16 (1960), 997.

22) B. Alper, H. Bøggild, P. Booth, L.J. Carroll, G. von Dardel, G. Damgaard, B. Duff, K. Hansen, N. Jackson, G. Jarlskog, L. Jönsson, A. Klovning, L. Leistam, E. Lillethun, S. Olgaard-Nielsen, M. Prentice, S. Sharrock and J.M. Weiss, Contribution No. 227 (unpublished) to Session A3 of the 17th Internat. Conf. on High-Energy Physics, London, 1974; See also B. Alper, H. Bøggild, P. Booth, L.J. Carroll, G. von Dardel, G. Damgaard, B. Duff, J.N. Jackson, G. Jarlskog, L. Jönsson, A. Klovning, L. Leistam, E. Lillethun, S. Olgaard-Nielsen, M. Prentice and J.M. Weiss, Nuclear Phys. B87 (1975), 19.

23) G. Bellettini, Proc. of the 8th Rencontre de Moriond, Méribel-les-Allues, France, 1973 (Ed. J. Tran Thanh Van, Orsay, France 1973), Vol. 2, p. 35.

24) G.R. Farrar and S.C. Frautschi, Phys. Rev. Letters 36 (1976), 1017.

25) V. Abramov, N. Anisimova, G. Bondarenko, V. Gridasov, Yu. Dobretsov, B. Dolgoshein, A. Dunaitzev, A. Dyshkant, V. Kantserov, V. Kirillov-Ugryumov, A. Kiselev, V. Kryshkin, P. Nevski, Yu. Nikitin, Yu. Rodnov, V. Senko, S. Somov and R. Sulyaev, as presented by S. Nurushev, page V-52 *in* Proc. 17th Internat. Conf. on High-Energy Physics, London,1974 (Ed. J.R. Smith) (Rutherford Laboratory, Chilton, Didcot, UK, 1975); see also B.A. Dolgoshein, Yu. Nikitin, G.V. Rozhnov, JETP Letters 22 (1975), 381.

26) J.P. Boymond, R. Mermod, P.A. Piroué, R.L. Sumner, J. Cronin, H.J. Frisch and M.J. Shochet, Phys. Rev. Letters 33 (1974), 112.

27) J.A. Appel, M.H. Bourquin, I. Gaines, D.C. Hom, L.M. Lederman, H.P. Paar, J.-P. Repellin, D.H. Saxon, H.D. Snyder, J.M. Weiss, J.K. Yoh, B.C. Brown, J.-M. Gaillard and T. Yamanouchi, Phys. Rev. Letters 33 (1974), 722.

28) L.B. Leipuner, R.C. Larsen, L.W. Smith, R.K. Adair, H. Kasha, C.M. Ankenbrandt, R.J. Stefanski and P.J. Wanderer, Phys. Rev. Letters 34 (1975), 103.
D. Bintinger, J. Curry, J. Pilcher, C. Rubbia, L. Sulak, W. Ford, A.K. Mann, D. Cline, R. Imlay and P. Wanderer, Phys. Rev. Letters 35 (1975), 72;
K. Winter, Phys. Letters 57B (1975), 479;
A.S. Akimenko, V.I. Belousov, A.M. Blik, N.I. Golovnya, V.M. Kutin, S.A. Zelepukin, G.P. Makarov, V.A. Sergeev, Yu.N. Simonov and V.P. Sugonyaev, JEPT Letters 22 (1975), 482;
L.B. Leipuner, R.C. Larsen, R.K. Adair, P.D. Bergey, A.B. Carter, D.M. Grannan, H. Kasha, R.G. Kellogg and M.J. Lauterbach, Phys. Rev. Letters 35 (1975), 1613;
D. Buchholz, H.J. Frisch, M.J. Shochet, R.P. Johnson, R.L. Sumner, O. Fackler and S.L. Segler, Phys. Rev. Letters 36 (1976), 932.
E.W. Beier, R. Patton, K. Raychaudhuri, H. Takeda, R. Thern, R. Van Berg, H. Weisberg, M.L. Good, P.D. Grannis, K. Johnson and J. Kirz, submitted to Vanderbilt Conference, Nashville, Tenessee, March 1976.
L. Baum, M.M. Block, B. Couchman, J. Crawford, A. Derevshchikov, D. Dibitonto, I. Golutvin, H. Hilscher, J. Irion, A. Kernan, V. Kukhtin, J. Layter, W. Marsh, P. McIntyre, F. Muller, B. Naroska, M. Nussbaum, A. Orkin-Lecourtois, L. Rossi, C. Rubbia, D. Schinzel, B. Shen, A. Staude, G. Tarnopolsky and R. Voss, Phys. Letters 60B (1976), 485.

29) J.A. Appel, M.H. Bourquin, I. Gaines, D.C. Hom, L.M. Lederman, H.P. Paar, J.-P. Repellin, H.D. Snyder, J.M. Weiss, J. K. Yoh, B.C. Brown, C.N. Brown, J.-M. Gaillard, J.R. Sauer and T. Yamanouchi, Phys. Rev. Letters 35 (1975), 9.

30) J.J. Aubert, U. Becker, P.J. Biggs, J. Burger, M. Chen, G. Everhart, P. Goldhagen, J. Leong, P. Mantsch, T. McCorriston, T.G. Rhoades, M. Rhode, S.C.C. Ting, Sau Lan Wu, J.W. Glenn and Y.Y. Lee, Phys. Rev. Letters 33 (1974), 1404.

31) J.E. Augustin, A.M. Boyarski, M. Breidenbach, F. Bulos, J.T. Dakin, G.J. Feldman, G.E. Fischer, D. Fryberger, G. Hanson, B. Jean-Marie. R.R. Larsen, V. Lüth, H.L. Lynch, D. Lyon, C.C. Morehouse, J.M. Paterson, M.L. Perl, B. Richter, P. Rapidis, R.F. Schwitters, W.M. Tanenbaum, F. Vannucci, G.S. Abrams, D. Briggs, W. Chinowsky, C.E. Friedberg, G. Goldhaber, R.J. Hollebeek, J.A. Kadyk, B. Lulu, F. Pierre, G.H. Trilling, J.S. Whitaker, J. Wiss and J.E. Zipse, Phys. Rev. Letters 33 (1974) 1406.

32) G.S. Abrams, D. Briggs, W. Chinowsky, C.E. Friedberg, G. Goldhaber, R.J. Hollebeek, J.A. Kadyk, A. Litke, B. Lulu, F. Pierre, B. Sadoulet, G.H. Trilling, J.S. Whitaker, J. Wiss, J.E. Zipse, J.-E. Augustin, A.M. Boyarski, M. Breidenbach, F. Bulos, G.J. Feldman, G.E. Fischer, D. Fryberger, G. Hanson, B. Jean-Marie, R.R. Larsen, V. Luth, H.L. Lynch, D. Lyon, C.C. Morehouse, J.M. Paterson, M.L. Perl, B. Richter, P. Rapidis, R.F. Schwitters, W. Tanenbaum and F. Vannucci, Phys. Rev. Letters 33 (1974), 1453.

33) S.C.C. Ting, EPS Internat. Conf. on High-Energy Physics, Palermo, Italy, June 1975.

34) B. Knapp, W. Lee, P. Leung, S.D. Smith, A. Wijangco, J. Knauer, D. Yount, D. Nease, J. Bronstein, R. Coleman, L. Cormell, G. Gladding, M. Gormley, R. Messner, T. O'Halloran, J. Sarracino, A. Wattenberg, D. Wheeler, M. Binkley, R. Orr, J. Peoples and L. Read, Phys. Rev. Letters 34 (1975), 1044.

35) G.J. Blanar, C.F. Boyer, W.L. Faissler, D.A. Garelick, M.W. Gettner, M.J. Glaubman, J.R. Johnson, H. Johnstad, M.L. Mallary, E.L. Pothier, D.M. Potter, M.T. Ronan, M.F. Tautz, E. von Goeler and R. Weinstein, Phys. Rev. Letters 35, (1975), 346;

K.J. Anderson, G.G. Henry, K.T. McDonald, J.E. Pilcher, E.I. Rosenberg, J.G. Branson, G.H. Sanders, A.J.S. Smith and J.J. Thaler, Phys. Rev. Letters 36, (1976), 237;

E. Nagy, M. Regler, W. Schmidt-Parzefall, K.R. Schubert, K. Winter, A. Brandt, H. Dibon, G. Flügge, F. Niebergall, P.E. Schumacher, C. Broll, G. Coignet, J. Favier, M. Vivargent, H. Eichinger, Ch. Gottfried and G. Neuhofer, Phys. Letters 60B (1975), 96;

Yu.M. Antipov, V.A. Bessubov, N.P. Budanov, Yu.B. Bushnin, S.P. Denisov, Yu.P. Gorin, A.A. Lebedev, A.A. Lednev, Yu.M. Mikhailov, A.I. Petrukhin, S.A. Polovnikov, V.N. Roinishvili, V.S. Selesnev, V.I. Sergienko, D.A. Stoyanova, A.N. Sytin, Ya.A. Vazdik and F.A. Yotch, Phys. Letters 60B (1976), 309;

H.D. Snyder, D.C. Hom, L.M. Lederman, H.P. Paar, J.M. Weiss, J.K. Yoh, J.A. Appel, B.C. Brown, C.N. Brown, W.R. Innes, T. Yamanouchi and D.M. Kaplan, Phys. Rev. Letters 36 (1976), 1415.

Table 1

Table of events and luminosities

$\sqrt{s}$ (GeV)	23.5	30.6	44.8	52.7 Low thresh.	52.7 Total	62.4	Description
Luminosity summary							
Integrated luminosity (10^{35} cm^{-2})	0.29	2.98	4.69	3.28	8.77	1.27	
Accepted events - single electron cuts							
Sample E	3	40	107	70	*190*	34	e^-, $p_T^* > 1.6$
	4	31	76	75	*213*	36	e^+, $p_T^* > 1.6$
	11	*125*	*302*	*244*	583 c)	*93*	e^-, $p_T^* > 1.3$
	9	*81*	*228*	*217*	515 c)	*85*	e^+, $p_T^* > 1.3$
Other data samples							
Sample A	-	386	761 a)	-	1887	157 b)	$p_T^* > 1.3$ No Čerenkov pulse-height cut
Sample B	-	-	1272 c)	-	2167 c)	-	$p_T^* > 1.0$
Sample C	-	-	995 c)	-	1811 c)		$p_T^* > 1.1$

Sample in italics is used for single electron cross-section.

a) 81.4% of full luminosity.

b) 49% of full luminosity.

c) Sample includes data with a threshold bias.

Table 2

Summary of contribution of backgrounds from charged hadrons, photon conversions and Dalitz decays to the sample of single electron events (all cuts) at $\sqrt{s}$ = 52.7 GeV and $p_T^* \geq 1.6$ GeV/c

Background	Contribution in % of accepted events
Charged hadrons	18.6 ± 1.9
γ-ray conversions	9.1 ± 3.1
Dalitz decays	20.7 ± 2.5
TOTAL	48.4 ± 4.4

Table 3

Observed e^+e^- mass distribution in the Arm 2 spectrometer for the sample of 2806 events (Table 1, Sample C) with all single electron cuts except that $p_T^* \geq 1.1$ GeV/c . The distribution of like charged electron pairs, assumed to be background is also given.

m_{ee}(GeV/c^2)	0.001-0.10	0.10-0.20	0.20-0.30	0.30-0.60	$\geq$ 0.600
e^+e^- pairs	12	4	5	1	1
e^+e^+ or e^-e^- pairs	0	5	0	0	0

Table 4

Relative yield of selected hadron events. The relative yield is defined as the ratio of selected hadron events to single electron events in a given p_T^* bin, integrated over all values of $\sqrt{s}$.

p_T^* interval	1.3-1.4	1.4-1.5	1.6-1.7	1.9-2.3	2.3-2.7	2.7-3.2
Relative yield	0.89 ± 0.07	0.96 ± 0.08	0.94 ± 0.08	1.07 ± 0.12	0.65 ± 0.15	0.48 ± 0.18

Table 5

p_T^* extrapolation of hadron background

	Background in % of accepted events		
p_T^* range (GeV/c)	1.3-1.4	1.6-1.7	2.3-2.7
All random	18.6	18.6	18.6
Equal knock-on and random	14.3	16.9	20.9
All knock-on	10.0	15.2	23.2
Average	14.3 ± 3.0	16.9 ± 1.2	20.9 ± 1.6

Table 6

Ratio of single electron events to selected conversions in each p_T^* bin for each value of $\sqrt{s}$. Also shown is the value of this ratio, integrated for $p_T^* \geq 1.3$ at each $\sqrt{s}$.

p_T^* (GeV/c) \ $\sqrt{s}$ (GeV)	23.5	30.6	44.8	52.7	62.4
1.0-1.1	0.05 ± 0.02	0.11 ± 0.01	0.14 ± 0.01	0.12 ± 0.01	0.15 ± 0.02
1.1-1.2	0.08 ± 0.02	0.11 ± 0.01	0.13 ± 0.01	0.12 ± 0.01	0.12 ± 0.02
1.2-1.3	0.11 ± 0.04	0.10 ± 0.01	0.15 ± 0.01	0.13 ± 0.01	0.14 ± 0.02
1.3-1.4	0.18 ± 0.03	0.12 ± 0.02	0.14 ± 0.01	0.14 ± 0.01	0.14 ± 0.02
1.4-1.5	0.08 ± 0.06	0.14 ± 0.02	0.14 ± 0.02	0.15 ± 0.01	0.16 ± 0.03
1.5-1.6	0.05 ± 0.05	0.14 ± 0.03	0.14 ± 0.02	0.16 ± 0.02	0.12 ± 0.04
1.6-1.7	0.11 ± 0.11	0.13 ± 0.03	0.11 ± 0.02	0.17 ± 0.02	0.14 ± 0.04
1.7-1.9	0.50 ± 0.20	0.17 ± 0.03	0.15 ± 0.02	0.14 ± 0.02	0.15 ± 0.05
1.9-2.3	0.40 ± 0.30	0.14 ± 0.04	0.16 ± 0.03	0.16 ± 0.02	0.17 ± 0.05
2.3-2.7		0.32 ± 0.1	0.21 ± 0.06	0.26 ± 0.07	0.17 ± 0.09
2.7-3.2		0.18 ± 0.14	0.56 ± 0.3	0.53 ± 0.2	0.30 ± 0.4
3.2-4.7			0.30 ± 0.2	0.31 ± 0.2	
Integrated for $p_T^* > 1.3$	0.16 ± 0.04	0.136 ± 0.009	0.147 ± 0.007	0.154 ± 0.005	0.147 ± 0.014

Table 7

Photon conversion and Dalitz decay background at $\sqrt{s}$ = 52.7 for various values of p_T^*

p_T^* (GeV/c)	1.0-1.1	1.3-1.4	1.6-1.7	2.3-2.7
Background as % of accepted events	55.3 ± 4.7	38.5 ± 2.9	28.1 ± 3.5	16.8 ± 4.9
Background as % of accepted events if $\eta^0/\pi^0 = 0$	45.6 ± 3.9	30.7 ± 2.3	21.8 ± 2.7	12.8 ± 3.7

Table 8

Detection efficiency for single electrons

Cut applied	Efficiency for electrons
Scintillator bits (3 planes)	0.890
Track fitting with requirement of spark in SC 1	0.85 ± 0.015
H_1' requirement:	
-self-vetoing	0.90 ± 0.02
-Landau tail	0.85 ± 0.02
$0.7 \leq p/E \leq 1.3$ (Resolution only)	0.92 ± 0.02
Čerenkov bit efficiency	0.87 ± 0.08
Čerenkov pulse-height cut, given that bit is set	0.78 ± 0.02
TOTAL	0.36 ± 0.04

Table 9

Corrections to the data. Uncorrected data to be multiplied by the factor given in the table. Correction used for all $\sqrt{s}$ and $p_T^* = 1.00 \pm 0.01$.

p_T^* (GeV/c)	1.3-1.4	2.3-2.7
Radiation in material preceding magnet	1.064 ± 0.007	1.064 ± 0.007
Spectrum shift from energy resolution	0.962 ± 0.01	0.93 ± 0.01
Compton background	0.98	0.99
TOTAL	1.003	0.98

Table 10

Inclusive cross-section computation at $\sqrt{s}$ = 52.7 GeV. Note that the integrated luminosities for $p_T^* > 1.6$ GeV/c and $p_T^* \leq 1.6$ GeV/c are different, as explained in the text.

p_T^* (GeV/c)	1.3-1.4	1.6-1.7	2.3-2.7
Accepted events	66	122	39
Selected conversion events	471	719	151
Conversion and Dalitz background (events)	25.4 ± 1.9	34.3 ± 4.3	6.5 ± 1.9
Charge hadron background (% of accepted events)	(14.3 ± 2.5)	(16.9 ± 3.0)	(20.9 ± 3.7)
Single electron signal (events)	31.2 ± 8.0	67.1 ± 10.1	24.3 ± 5.3
Raw cross-section (10^{-34} cm^2)	103.3 ± 24.5	31.8 ± 4.8	1.98 ± 0.43
$K^{\pm}$ (10^{-34} cm^2)	7.8	1.30	0.028
K^0 (10^{-34} cm^2)	3.0	0.54	0.012
Corrected cross-section (10^{-34} cm^2)	92.5 ± 25.9	30.0 ± 5.0	1.94 ± 0.43

Table 11

The charge-averaged invariant cross-sections for inclusive electron production as a funtion of $\sqrt{s}$ and p_T^*

p_T^* (GeV/c) \ $\sqrt{s}$ (GeV)	Invariant cross-section $E\frac{d^3\sigma}{dp^3}$ (10^{-34} cm^2/GeV^2)				
	23.5	30.6	44.8	52.7	62.4
1.3-1.4	94.3 ± 52.1	36.6 ± 13.5	82.8 ± 15.7	92.5 ± 25.9	87.4 ± 28.2
1.4-1.5	2.5 ± 21.7	34.1 ± 10.9	50.0 ± 10.9	55.0 ± 17.0	59.2 ± 20.6
1.5-1.6	-5.5 ± 14.7	20.2 ± 7.7	32.3 ± 7.9	47.2 ± 13.9	36.7 ± 17.4
1.6-1.7	4.3 ± 12.0	11.8 ± 5.6	14.5 ± 5.4	30.0 ± 5.0	28.9 ± 13.1
1.7-1.9	19.7 ± 11.5	9.4 ± 3.1	13.7 ± 3.1	13.3 ± 2.4	18.4 ± 6.5
1.9-2.3	4.0 ± 3.5	1.99 ± 0.95	4.71 ± 1.13	4.95 ± 0.90	5.2 ± 2.3
2.3-2.7		1.46 ± 0.61	1.27 ± 0.49	1.94 ± 0.43	1.9 ± 1.2
2.7-3.2		0.19 ± 0.20	0.52 ± 0.22	0.68 ± 0.19	0.94 ± 0.61
3.2-4.7	-	-	0.055 ± 0.035	0.065 ± 0.030	-
	Integrated cross-section $\frac{d\sigma}{dy}$ ($p_T^* > 1.3$)(10^{-32} cm^2)				
	1.47 ± 0.61	1.36 ± 0.20	2.32 ± 0.21	2.82 ± 0.32	2.83 ± 0.43

Table 12

Systematic errors in over-all normalization

a) Inclusive electron measurement	
Luminosity	± 5%
Energy scale error (±3%)	±25%
Charged hadron background	± 3%
Detection efficiency	±11%
Other small corrections	± 1%
TOTAL	±28%
b) Electron/neutral pion ratio	
Energy scale error (±3%)	± 3%
Background (accepted events)	± 3%
Background (selected conversions)	± 1%
Relative detection efficiency	± 5.7%
Other small corrections	± 1%
TOTAL	± 7.3%

Table 13

The charged-averaged ratio $\left[(e^+ + e^-)/2\pi^0\right] \times 10^4$ as a function of $\sqrt{s}$ and p_T^*

p_T^* (GeV/c) \ $\sqrt{s}$ (GeV)	23.5	30.6	44.8	52.7	62.4
1.0-1.1	-0.72 ± 0.41	0.62 ± 0.25	1.39 ± 0.28	0.94 ± 0.29	1.65 ± 0.52
1.1-1.2	-0.03 ± 0.35	0.60 ± 0.21	1.05 ± 0.24	0.88 ± 0.25	0.85 ± 0.44
1.2-1.3	0.53 ± 0.62	0.48 ± 0.19	1.51 ± 0.22	1.18 ± 0.24	1.32 ± 0.41
1.3-1.4	1.54 ± 0.44	0.79 ± 0.32	1.26 ± 0.21	1.33 ± 0.22	1.29 ± 0.39
1.4-1.5	0.09 ± 0.70	0.98 ± 0.28	1.14 ± 0.32	1.37 ± 0.20	1.48 ± 0.50
1.5-1.6	-0.22 ± 0.52	0.91 ± 0.37	1.08 ± 0.30	1.47 ± 0.32	0.78 ± 0.60
1.6-1.7	0.41 ± 1.06	0.75 ± 0.34	0.63 ± 0.28	1.56 ± 0.31	1.05 ± 0.57
1.7-1.9	4.47 ± 2.03	1.17 ± 0.32	1.16 ± 0.27	1.09 ± 0.28	1.15 ± 0.67
1.9-2.3	2.7 ± 2.4	0.68 ± 0.35	1.10 ± 0.34	1.15 ± 0.24	1.18 ± 0.58
2.3-2.7	-	1.72 ± 0.66	1.27 ± 0.51	1.82 ± 0.64	0.80 ± 0.79
2.7-3.2	-	0.58 ± 0.69	3.98 ± 2.37	3.88 ± 1.64	1.50 ± 3.00
3.2-4.7	-	-	1.22 ± 1.02	1.34 ± 1.07	-

Table 14

95% confidence level upper limits for a particle of mass m, or a mass continuum, which decays to e^+e^- with branching ratio B, at $\sqrt{s}$ = 52.7 GeV/c. For a discrete particle the cross-section quoted is the integral of the invariant cross-section over azimuth and over all transverse momenta $p_T^* \geq 1.3$ GeV/c. For a continuum, the integral is also taken over the 0.100 GeV/c^2 mass bin centred on the quoted mass. Also given is the fraction of the observed single electron cross-section that would be caused by the quoted e^+e^- pair cross-section.

Mass (GeV/c^2)	$B \frac{d\sigma}{dy}$ ($p_T^* > 1.3$ GeV/c) (cm^2)	Fraction of single electron signal
0.400	5.54×10^{-33}	0.064
0.500	8.37×10^{-33}	0.104
0.600	1.64×10^{-32}	0.178
0.700	3.45×10^{-32}	0.512
0.800	1.08×10^{-31}	1.61
0.900	1.77×10^{-31}	2.73
1.000	2.65×10^{-31}	4.45

Table 15

Angular apertures and kinematic cuts in the centre-of-mass system, for the two triggers used in the search for opposite-side e^+e^- pairs

Trigger	Spectro-meter arm	θ^* (degrees)	ϕ^* (degrees)	$\Delta\Omega^*$ (sr)	p_T^* cut (GeV/c)
Arm 1	1	90 ± 13.3	0 ± 4.7	0.075	$\geq$ 1.0
	2	90 ± 22.5	180 ± 7.2	0.192	$\geq$ 1.0
Arm 2	1	90 ± 13.3	0 ± 4.9	0.078	$\geq$ 1.0
	2	90 ± 22.5	180 ± 7.2	0.192	$\geq$ 1.3

Table 16

Kinematical parameters for the observed e^+e^- pairs

$\sqrt{s}$ (GeV)	$M(e^+e^-)$ (GeV/c^2)	p_T^* (GeV/c)	y
44.8	2.93	0.88	-0.165
52.7	2.99	0.78	-0.033
52.7	3.00	0.20	0.239
44.8	3.02	0.33	0.191
44.8	3.07	0.72	-0.007
52.7	3.07	0.30	0.157
30.5	3.12	0.32	0.318
44.8	3.18	0.33	0.095
52.7	3.29	1.43	-0.001
52.7	3.46	1.18	0.195
52.7	3.79	0.36	0.121

Table 17

Differential cross-section for the reaction

$$p + p \rightarrow J(3.1) + \text{anything}$$
$$\hookrightarrow e^+e^-$$

for various values of assumed $\langle p_T^* \rangle$

$\langle p_T^* \rangle$ (GeV/c)	$B_{ee} \times \left.\frac{d\sigma}{dy}\right\|_{y=0}$ $(p + p \rightarrow J + \text{anything})$ (cm^2)
0.67	$(7.5 \pm 2.5) \times 10^{-33}$
1.0	$(1.2 \pm 0.4) \times 10^{-32}$
1.5	$(2.1 \pm 0.7) \times 10^{-32}$
2.0	$(3.2 \pm 1.1) \times 10^{-32}$

Figure captions

Fig. 1 : Plan view of apparatus.

Fig. 2 : Example of an identified e^+e^- pair event, which opens up in the magnet.

Fig. 3 : The number of events with all cuts applied, except momentum-energy agreement, plotted as a function of the ratio of the momentum p to the energy E deposited in the lead-glass array. Curve a corresponds to all accepted events; curve b to charged hadrons without the Čerenkov counter bit requirement and curve c corresponds to a pure sample of electrons. Curves b and c are normalized so that their sum gives the best fit to curve a.

Fig. 4 : Curve a is the yield of accepted events plotted as a function of the number of radiation lengths t of material before the first spark chamber. The data are normalized to the results obtained under normal running conditions. Also shown, curve b, plotted in the same manner, is the total yield when photon conversions and Dalitz decays are selected. The data points with dashed error bars have been corrected for radiation in the material preceeding the magnet.

Fig. 5 : Distribution of e^+e^- pairs observed in the Arm 2 spectrometer for the event sample with no H_1' cut and no Č pulse-height cut. Also shown is the event distribution when the $H_1' \leq 1.5$ cut is applied.

Fig. 6 : Centre-of-mass system rapidity distribution of single electron events. The shape of the geometrical acceptance is also shown.

Fig. 7 : The charge-averaged invariant cross-section for electron production, plotted as a function of the centre-of-mass momentum p_T^* for five values of $\sqrt{s}$. The curve represents a fit of the charge-averaged pion data of the BS Collaboration[22], and has been multiplied by 10^{-4}.

Fig. 8 : a) The ratio of the charge-averaged invariant electron cross-section to the BS fit[22].

b) The ratio of electrons to neutral pions plotted as a function of p_T^* for four values of $\sqrt{s}$. The pion data were obtained from the selected conversion spectrum measured in this experiment, as explained in the text.

Fig. 9 : The ratio of the invariant cross-sections of electrons to pions of $p_T^* \geq 1.3$ GeV/c plotted as a function of c.m.s. energy $\sqrt{s}$. The pion data were obtained from the work of the Bristish-Scandinavian Collaboration[22] (solid points) and from the spectrum of selected conversions measured in this experiment (open points). The two curves shown are fits to the solid points.

Fig. 10 : The number of charged hadrons, per steradian, per GeV/c, observed in association with either a single electron event or selected conversion, of transverse momentum $p_T^* \geq 1.1$ GeV/c, in the same-side spectrometer. No correction has been made for the bias introduced by the H_1' cut.

Fig. 11 : The number of particles, per GeV/c, per steradian, observed in association with either a single electron event or selected conversion of transverse momentum $p_T^* \geq 1.0$ GeV/c, in the opposite spectrometer. A charged particle track is identified as a hadron if it fails to set the $\check{C}$ bit of the $\check{C}$erenkov cell through which it passed; otherwise it is called an electron.

Fig. 12 : Mass spectrum of hadrons observed in the spectrometer opposite to
a) a selected conversion or charged hadron;
b) a single electron.

Fig. 13 : a) Mass spectrum of all oppositely charged pairs observed in the special run, assuming that the particles are K^+K^-. The shaded data are cut for total momentum $p_{K^+K^-} \geq 1.6$ GeV/c.

b) Distribution of K^+K^- pairs with predicted total momentum ≥ 1.6 GeV/c, if $\sigma_{\phi^0} = 10\ \sigma_{\pi^0}$, the ϕ^0 rapidity distribution is flat for rapidity $|y| \leq 0.4$ and the transverse momentum distribution of ϕ^0 and π^0 are identical.

Fig. 14 : Acceptance probability for an e^+e^- pair of mass m to satisfy the $H_1' \leq 1.5$ pulse-height cut, given that one member of the pair satisfies all the other single electron cuts with $p_T^* > 1.6$ GeV/c (solid curve). The broken curve is the acceptance probability with the further restriction that the second track be fully reconstructed in the spectrometer. Assumptions used for these curves were that the particle of mass m be produced with a transverse momentum distribution given by the CCR fit[4] and decay to an e^+e^- pair with isotropic rest-frame angular distribution. A $1 + \cos^2 \theta^*$ angular distribution increases the acceptances at low masses by at most a factor of 1.5.

Fig. 15 : Invariant mass distribution for the observed e^+e^- pairs. The curves represent the shapes of the acceptance, as a function of the e^+e^- invariant mass value, for the Arm 1 and Arm 2 triggers, respectively.

Fig. 16 : Rapidity distribution of the observed e^+e^- pairs. The curve represents the shape of the apparatus acceptance, which is the same for both triggers.

Fig. 17 : A plot of the value of $B_{ee}\ d\sigma_J/dy$ at $y = 0$ measured in this experiment[2] compared with the measurements done by CHCIF [34] and transformed by us to be differential in rapidity. The dashed line is an artist's conception of the rapidity dependence of J(3.1) production.

Fig. 18 : The spectrum of single electrons predicted due to the production and decay of the J(3.1) for four assumed values of $\langle p_T^* \rangle$. The J(3.1) cross-section corresponding to these values of $\langle p_T^* \rangle$ are given in Table 17. Also shown is the charge-averaged invariant cross-section for single electron production at $\sqrt{s} = 52.7$ GeV from Table 11. The three lowest points come from the e/π^0 data, and have been renormalized so as to agree with the other data for $p_T^* > 1.3$ GeV/c.

Fig. 19 : a) Upper limits of e^+e^- or $e^\pm\nu$ production at $y = 0$ from single electron spectrum.

b) 95% confidence level upper limits for e^+e^- production at $y = 0$ from opposite side e^+e^- pairs.

Fig. 20 : The distribution of normalized SA counter amplitude as measured for
a) hadrons (wrong $\check{C}$ cell);
b) electrons (identified conversions).
The normalized SA amplitude is defined as the pulse amplitude in the SA counter, in units of the minimum ionization, divided by 6.0 p, an empirically determined value for electrons of laboratory momentum p (GeV/c).

Fig. 21 : The distribution of normalized SA counter amplitude for accepted events which satisfy all other cuts. The hadron background has been calculated using the curve of Fig. 20.

Fig. 22 : The charge-averaged spectrum of single electrons $(e^+ + e^-)/2$, averaged for $\sqrt{s} = 52.7$ GeV and $\sqrt{s} = 44.8$ GeV. The triangles are from the Arm 1 analysis and the circles are from the Arm 2 analysis. The solid line is the British-Scandinavian fit[22] for $(\pi^+ + \pi^-)/2$, times 10^{-4}.

Fig. 23 : The charge-averaged ratios $(e^+ + e^-)/(\pi^+ + \pi^-)$, averaged for $\sqrt{s}$ = 52.7 GeV, and $\sqrt{s}$ = 44.8 GeV. The data for the range $0.6 \leq p_T^* \leq 2.0$ GeV/c are from Arm 1 and for $1.3 \leq p_T^* \leq 4.5$ GeV/c from Arm 2.

PLAN VIEW OF APPARATUS

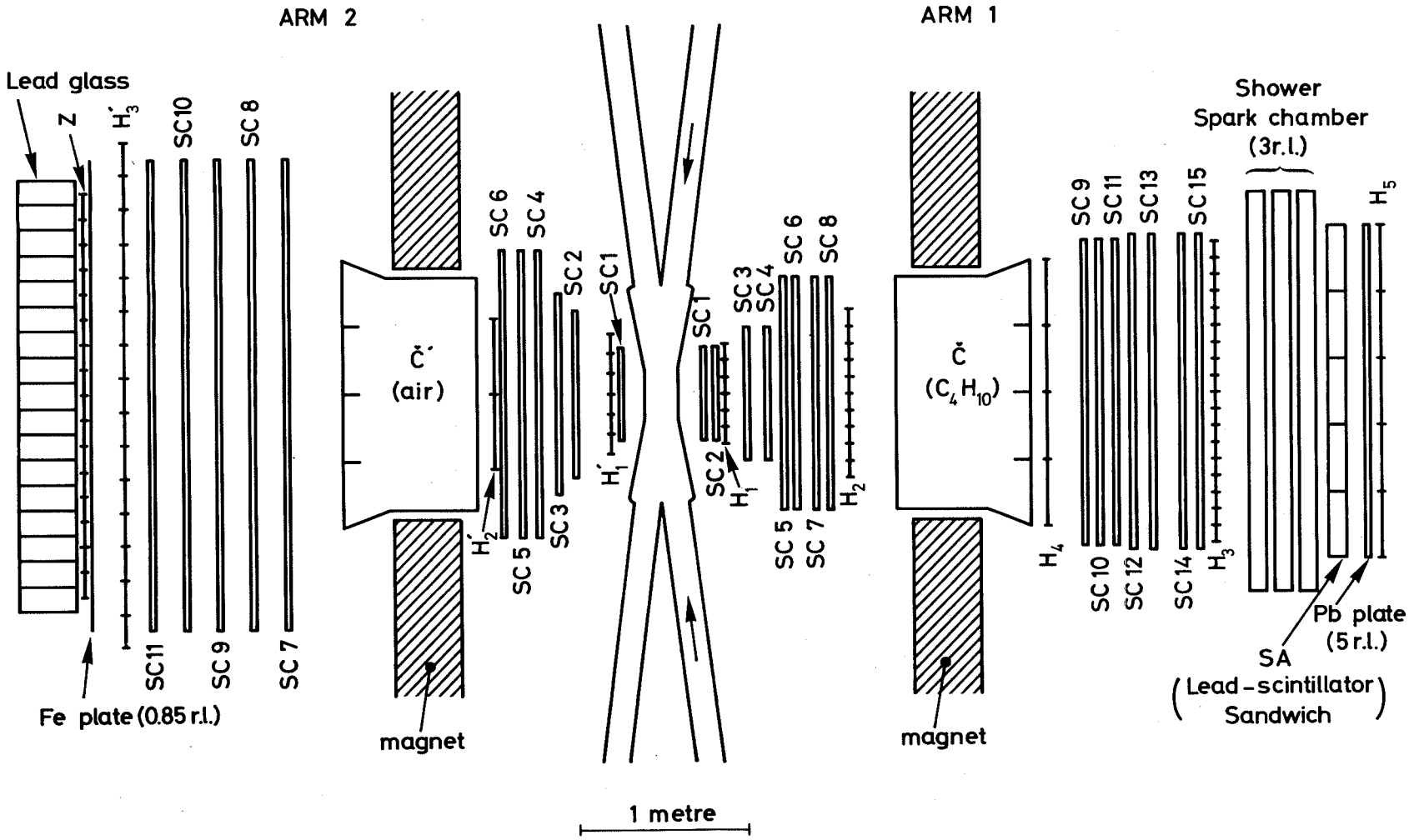

Fig. 1

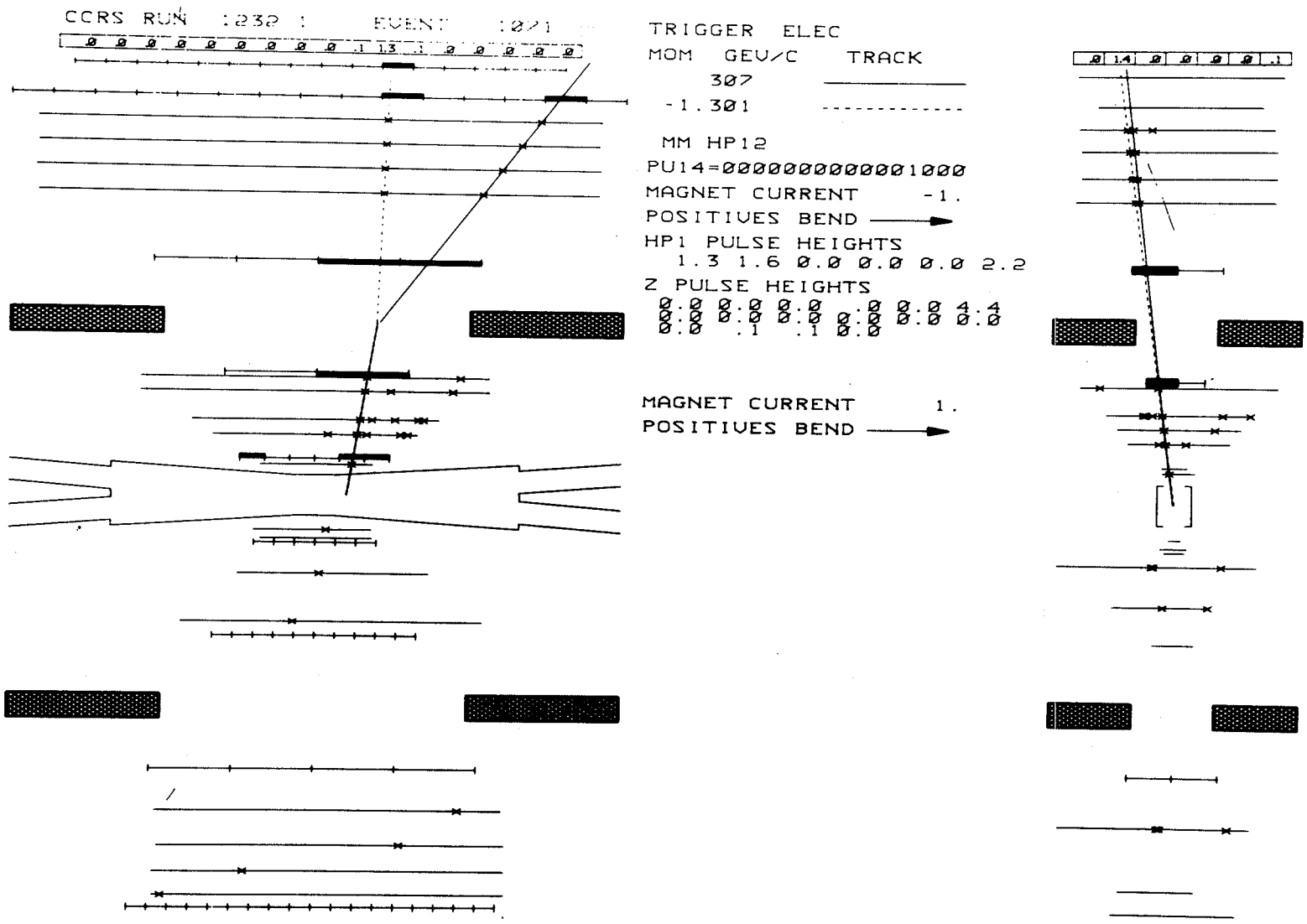
CCRS RUN 1232 1 EVENT 1021
TRIGGER ELEC
MOM GEV/C TRACK
307
-1.301
MM HP12
PU14=0000000000001000
MAGNET CURRENT -1.
POSITIVES BEND
HP1 PULSE HEIGHTS
1.3 1.6 0.0 0.0 0.0 2.2
Z PULSE HEIGHTS
MAGNET CURRENT 1.
POSITIVES BEND

Fig. 2

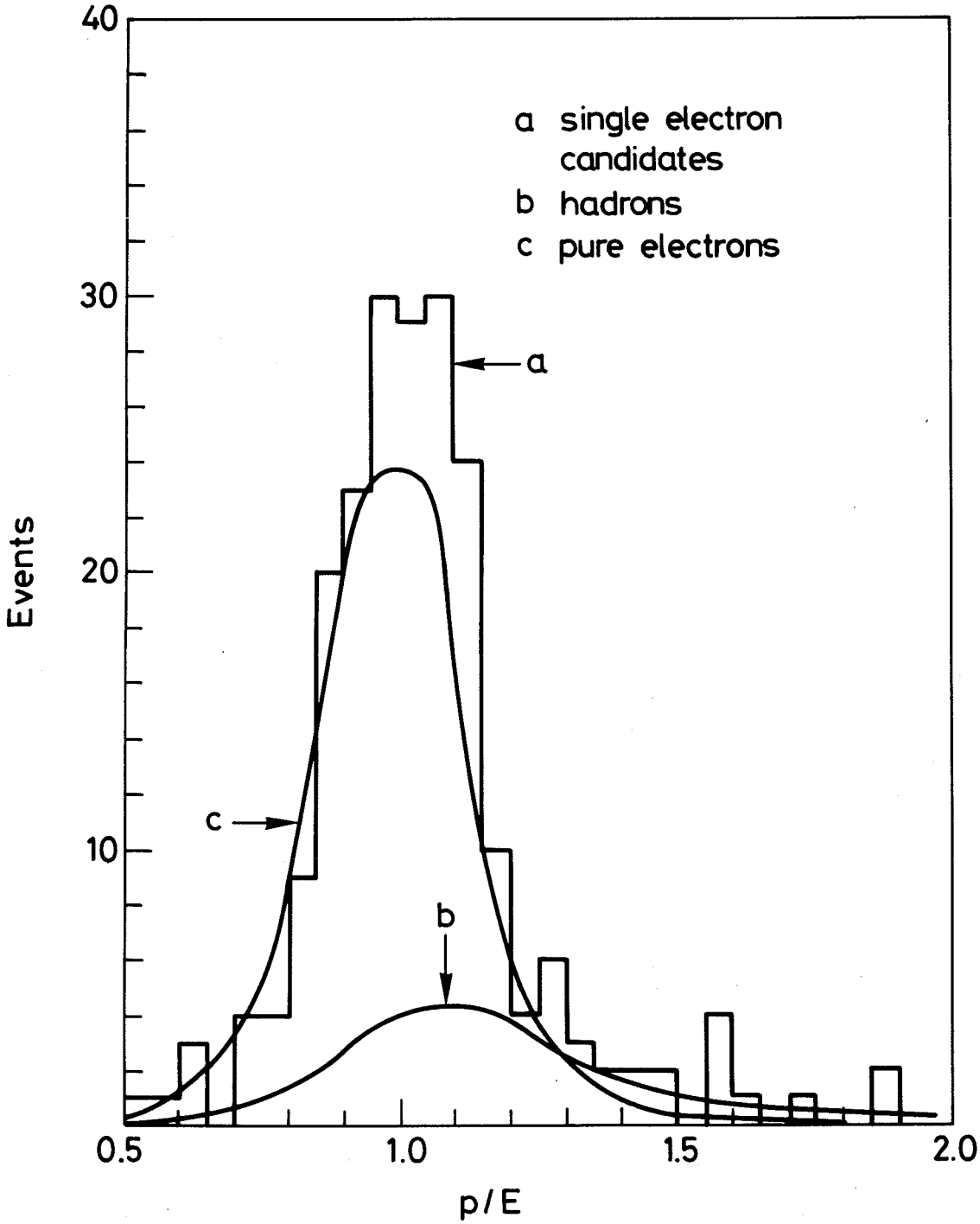
40
30
20
10
Events
a single electron candidates
b hadrons
c pure electrons
a
c
b
0.5
1.0
1.5
2.0
p/E

Fig. 3

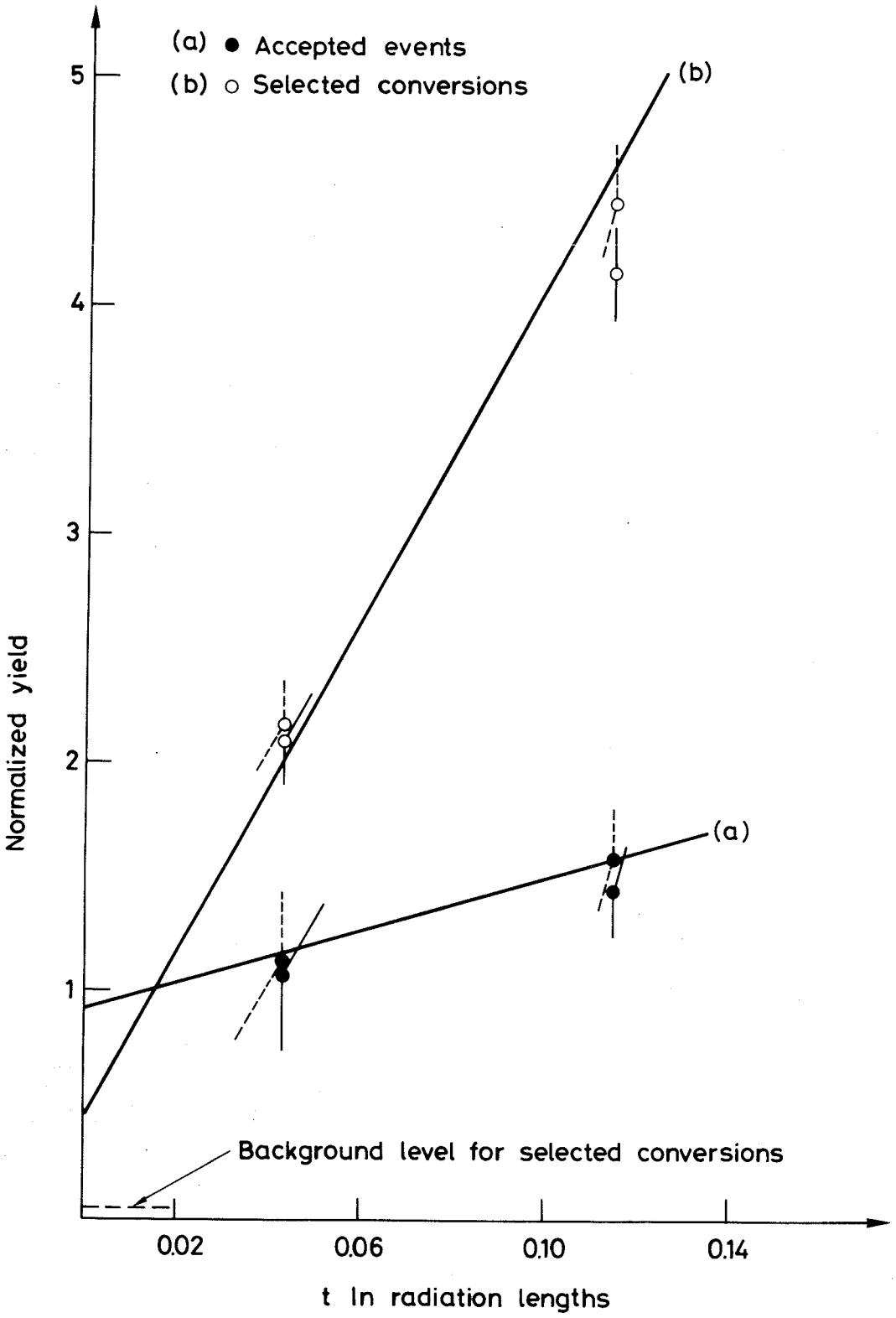
(a) ● Accepted events
(b) ○ Selected conversions
(b)
(a)
Normalized yield
5
4
3
2
1
Background level for selected conversions
0.02
0.06
0.10
0.14
t In radiation lengths

Fig. 4

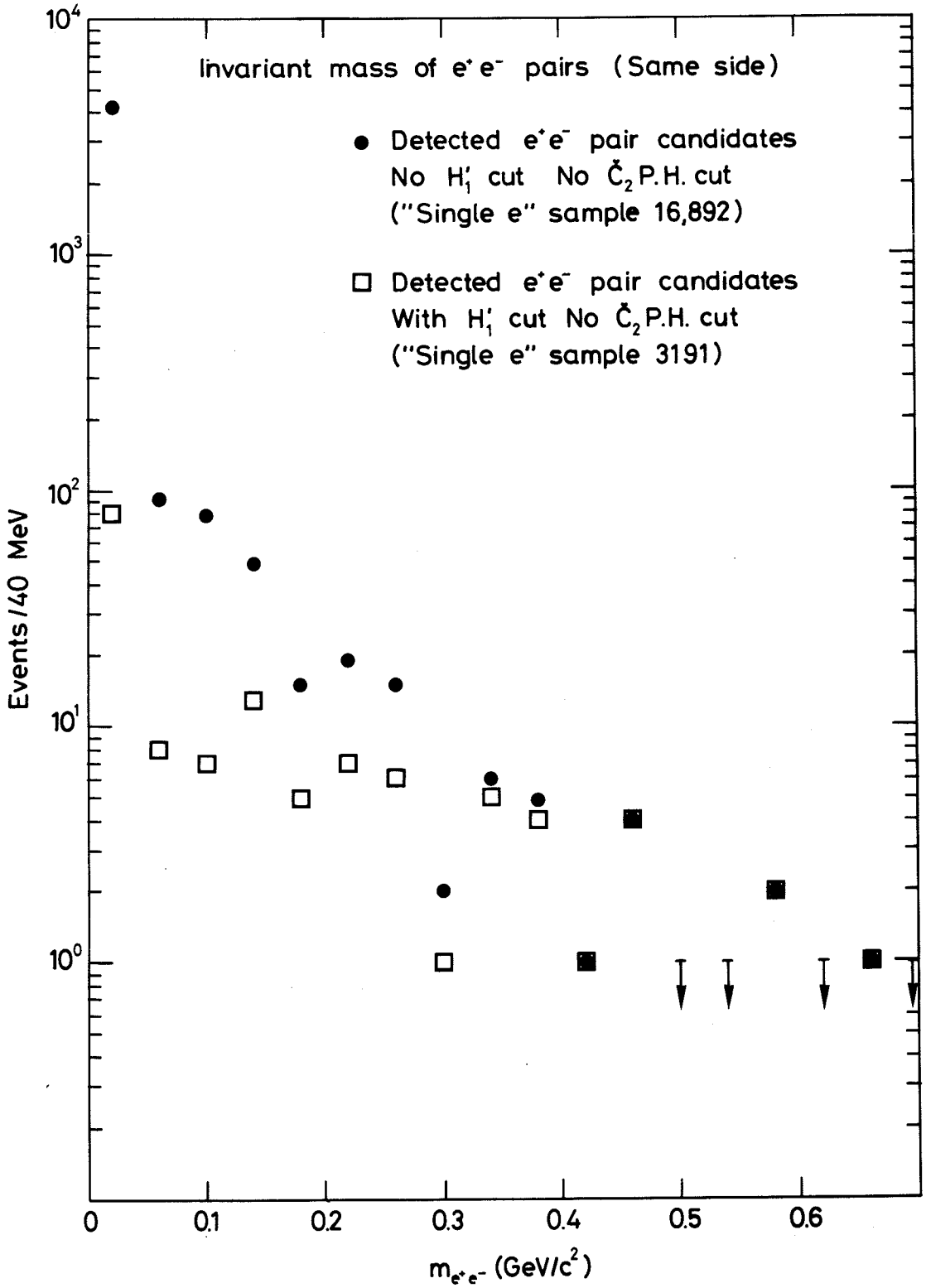
Invariant mass of e⁺e⁻ pairs (Same side)
Detected e⁺e⁻ pair candidates
No H₁' cut No Č₂ P.H. cut
("Single e" sample 16,892)
Detected e⁺e⁻ pair candidates
With H₁' cut No Č₂ P.H. cut
("Single e" sample 3191)
Events/40 MeV
10⁴
10³
10²
10¹
10⁰
0
0.1
0.2
0.3
0.4
0.5
0.6
m_{e⁺e⁻} (GeV/c²)

Fig. 5

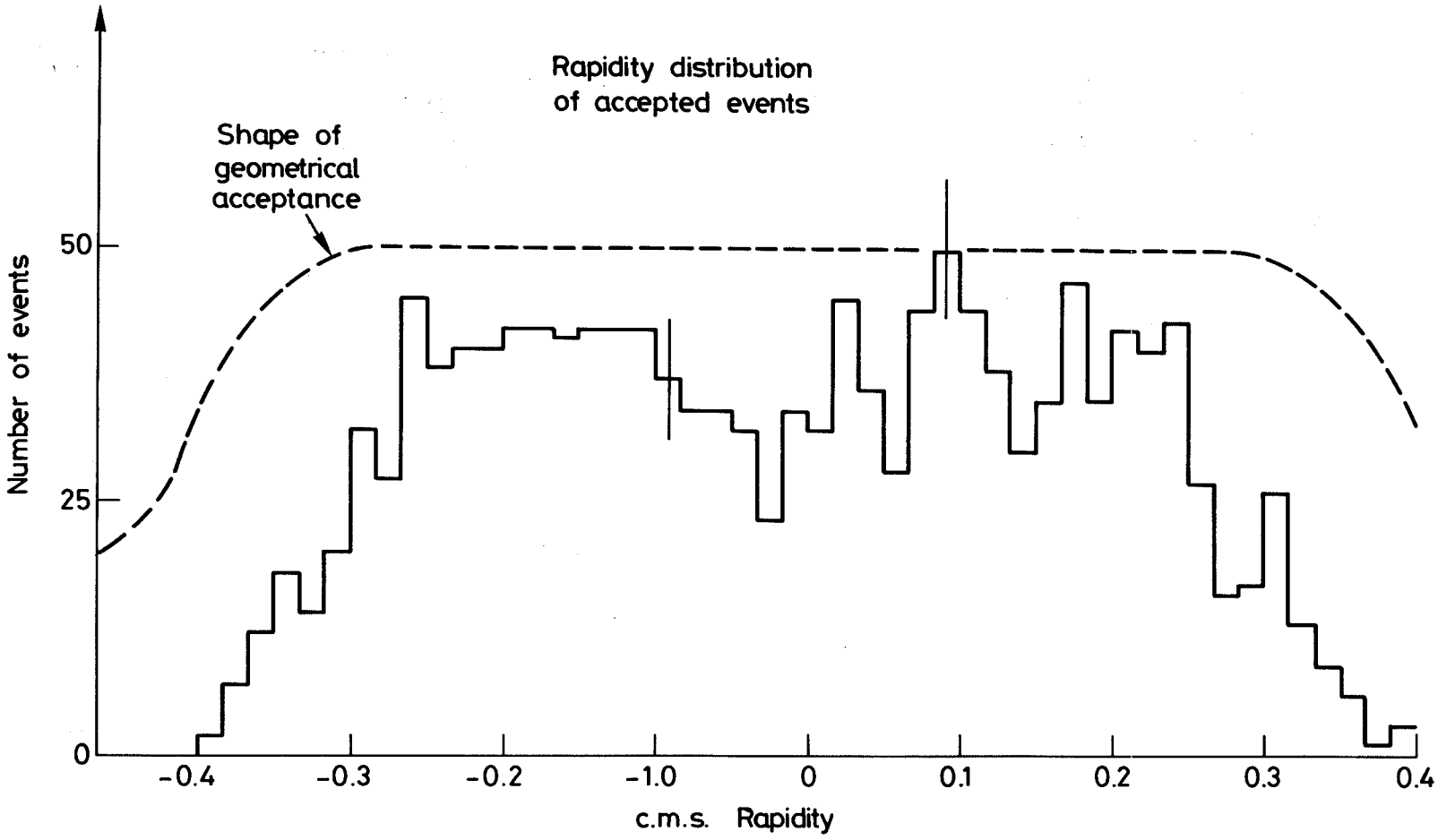
Rapidity distribution
of accepted events
Shape of
geometrical
acceptance
Number of events
50
25
0
-0.4
-0.3
-0.2
-1.0
0
0.1
0.2
0.3
0.4
c.m.s. Rapidity

Fig. 6

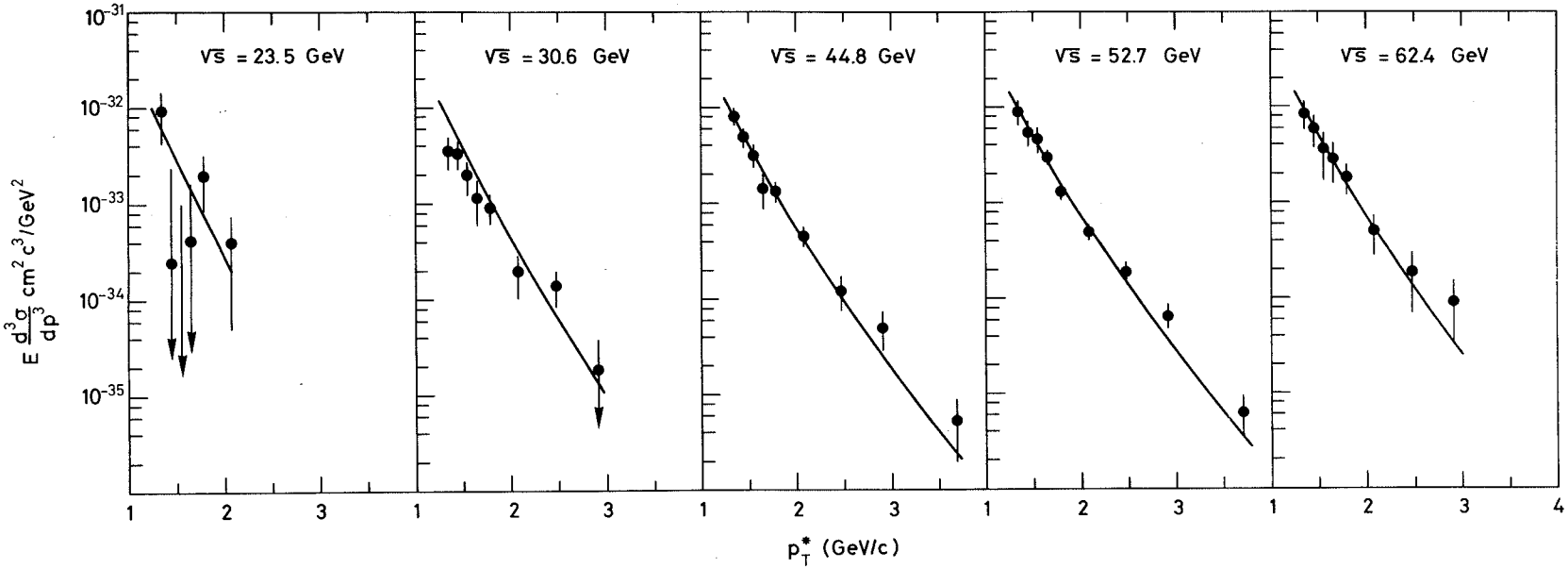
$E\frac{d^3\sigma}{dp^3}$ cm^2 c^3/GeV^2
10^{-31}
10^{-32}
10^{-33}
10^{-34}
10^{-35}
$\sqrt{s}$ = 23.5 GeV
$\sqrt{s}$ = 30.6 GeV
$\sqrt{s}$ = 44.8 GeV
$\sqrt{s}$ = 52.7 GeV
$\sqrt{s}$ = 62.4 GeV
1
2
3
4
p_T^* (GeV/c)

Fig. 7

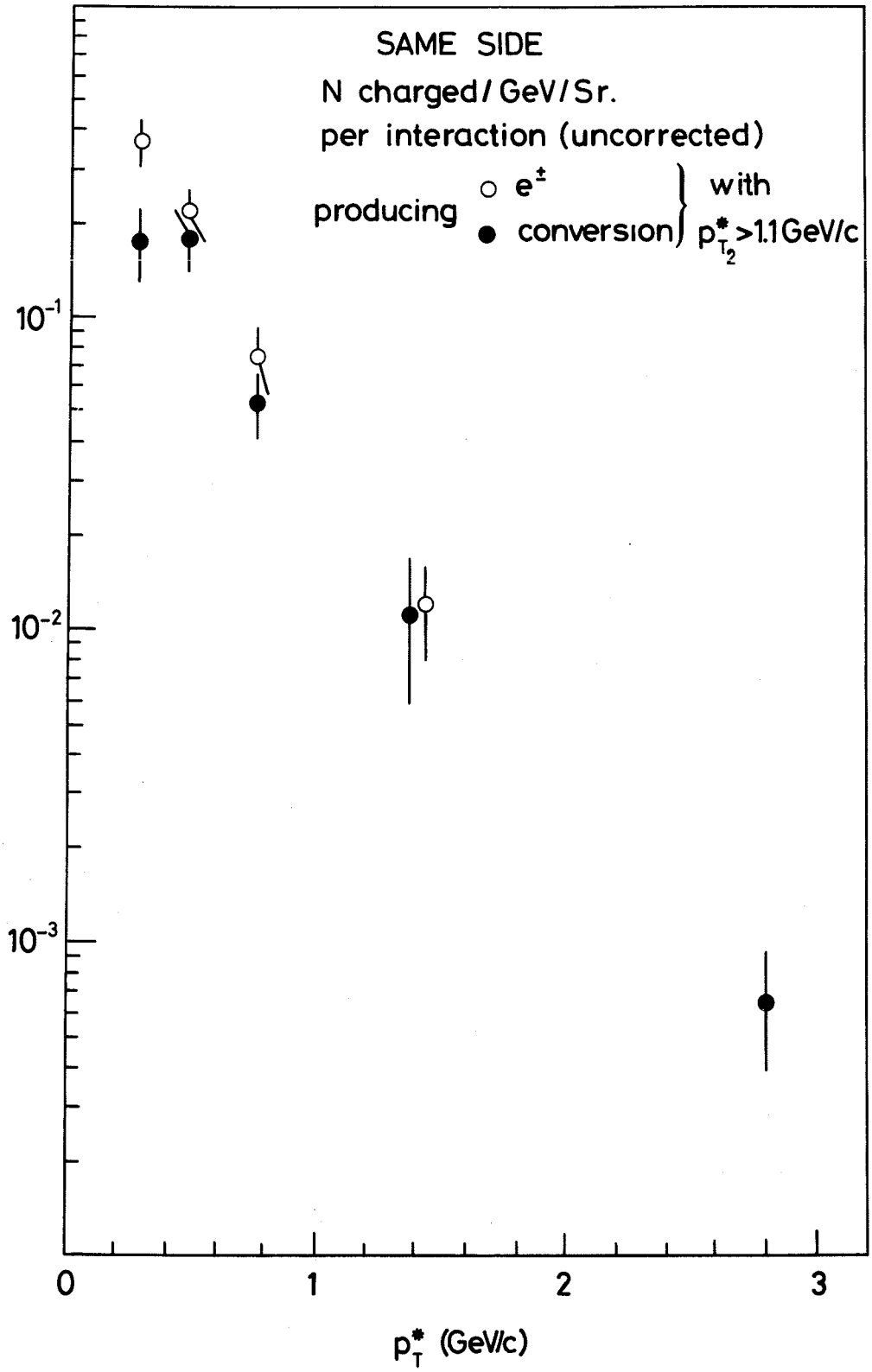
SAME SIDE
N charged / GeV / Sr.
per interaction (uncorrected)
producing
○ e±
● conversion
with
p*T2 > 1.1 GeV/c
10-1
10-2
10-3
0
1
2
3
p*T (GeV/c)

Fig. 10

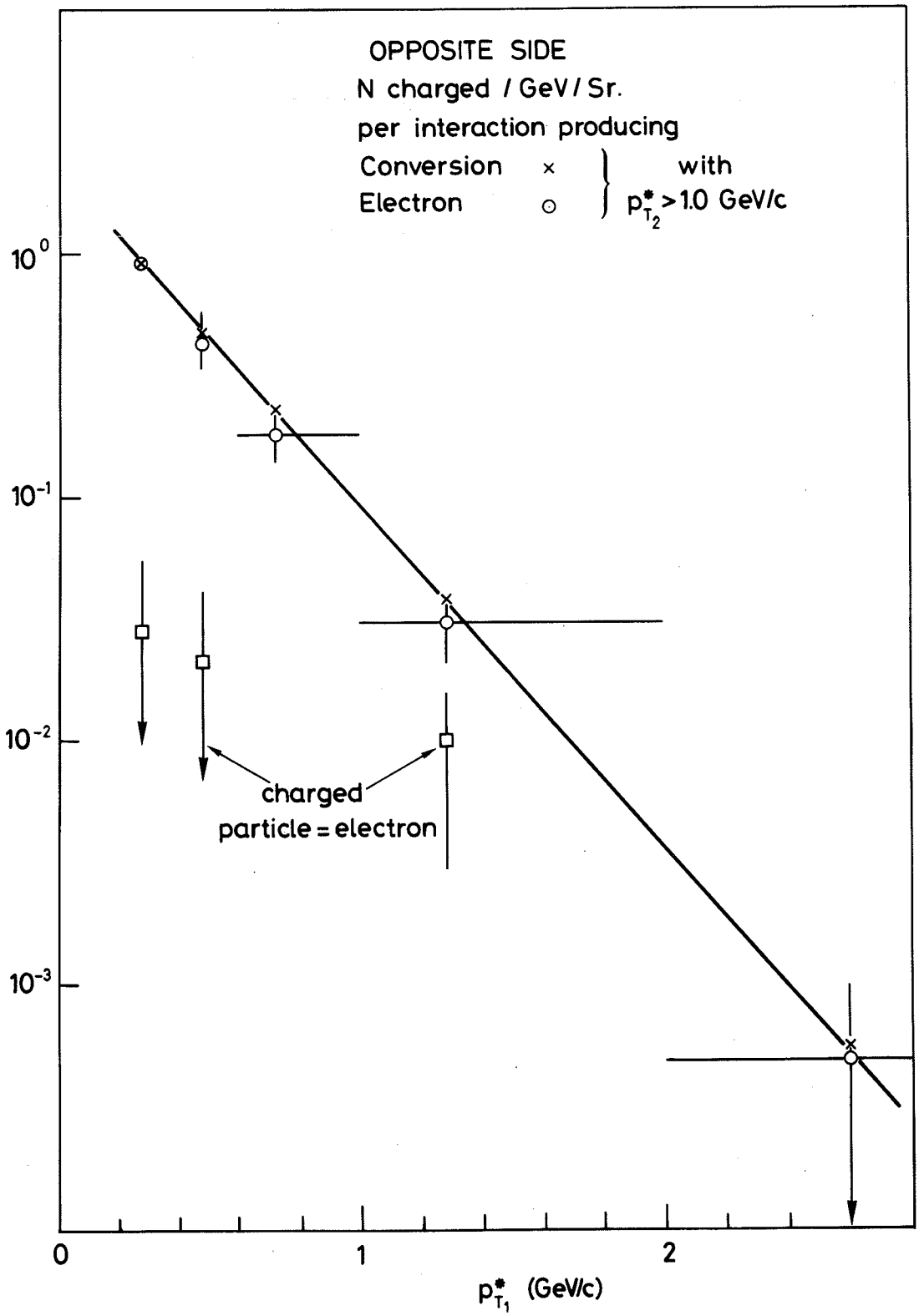
OPPOSITE SIDE
N charged / GeV / Sr.
per interaction producing
Conversion ×
Electron ⊙
with
$p^*_{T_2}$ > 1.0 GeV/c
10^0
10^{-1}
10^{-2}
10^{-3}
charged
particle = electron
0
1
2
$p^*_{T_1}$ (GeV/c)

Fig. 11

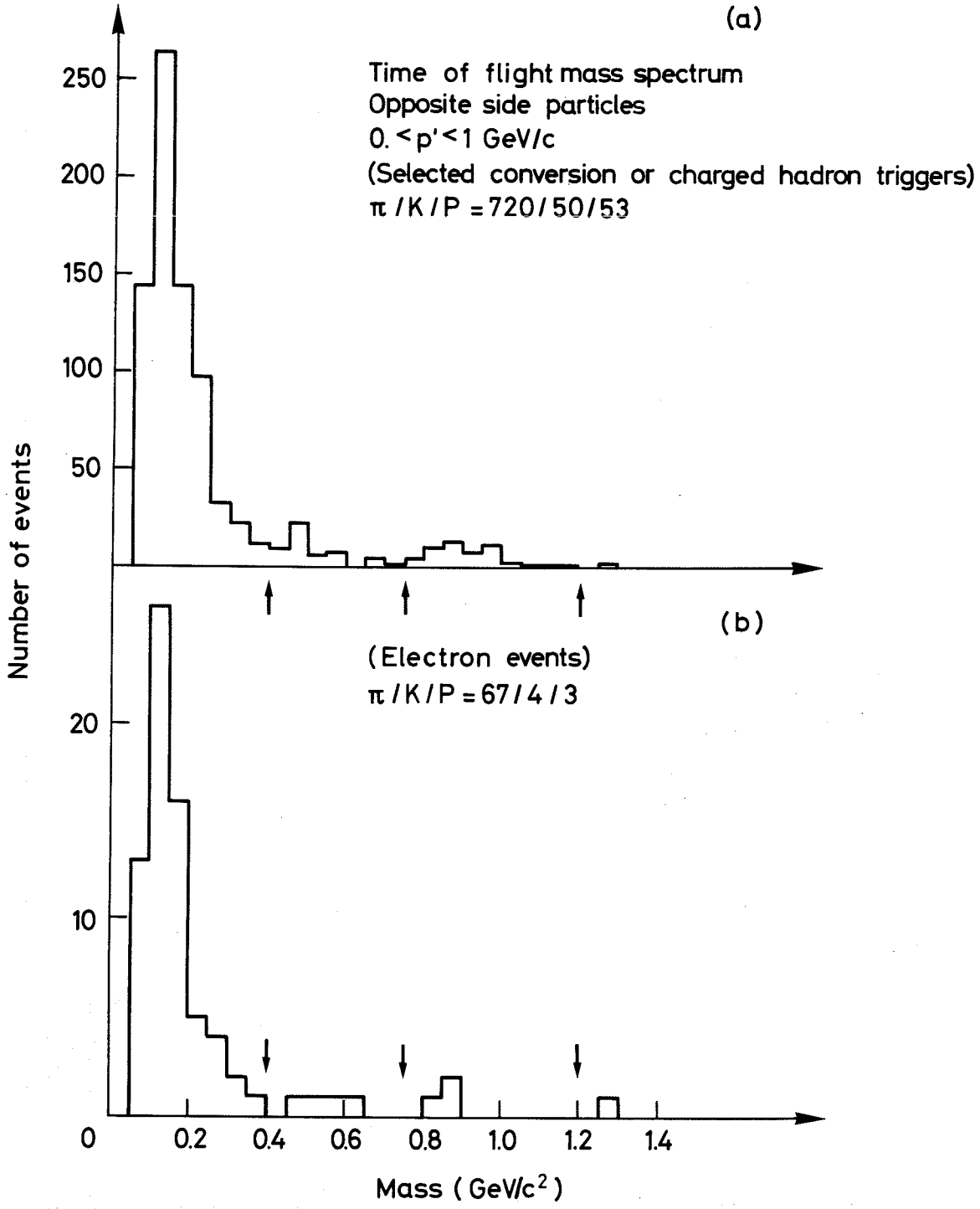
(a)
Time of flight mass spectrum
Opposite side particles
0. < p' < 1 GeV/c
(Selected conversion or charged hadron triggers)
π / K / P = 720 / 50 / 53
(b)
(Electron events)
π / K / P = 67 / 4 / 3
Number of events
250
200
150
100
50
20
10
0
0.2
0.4
0.6
0.8
1.0
1.2
1.4
Mass (GeV/c²)

Fig. 12

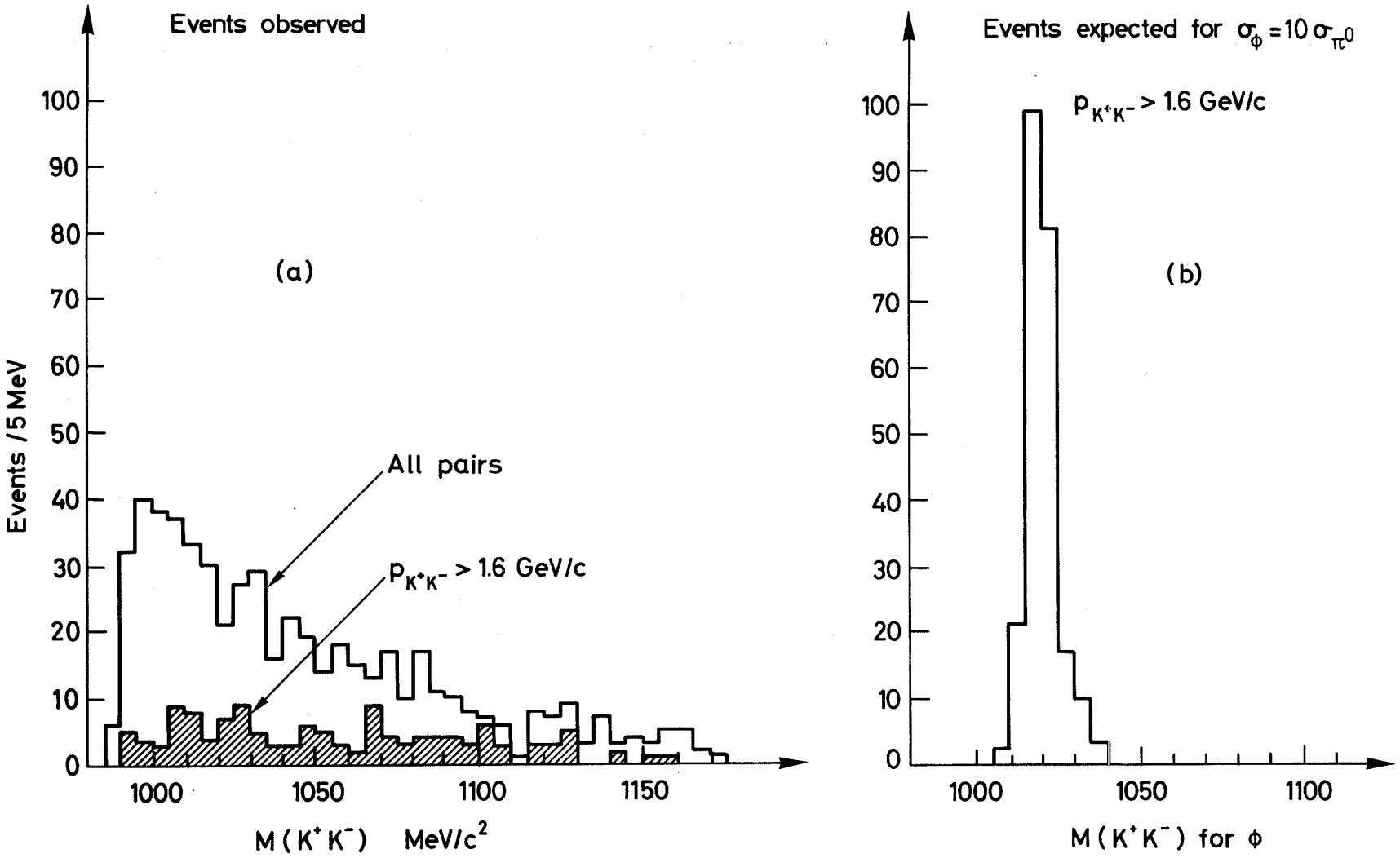
Events observed
(a)
All pairs
$p_{K^+K^-} > 1.6$ GeV/c
Events /5 MeV
$M(K^+K^-)$ MeV/c^2
Events expected for $\sigma_\phi = 10\,\sigma_{\pi^0}$
$p_{K^+K^-} > 1.6$ GeV/c
(b)
$M(K^+K^-)$ for ϕ

Fig. 13

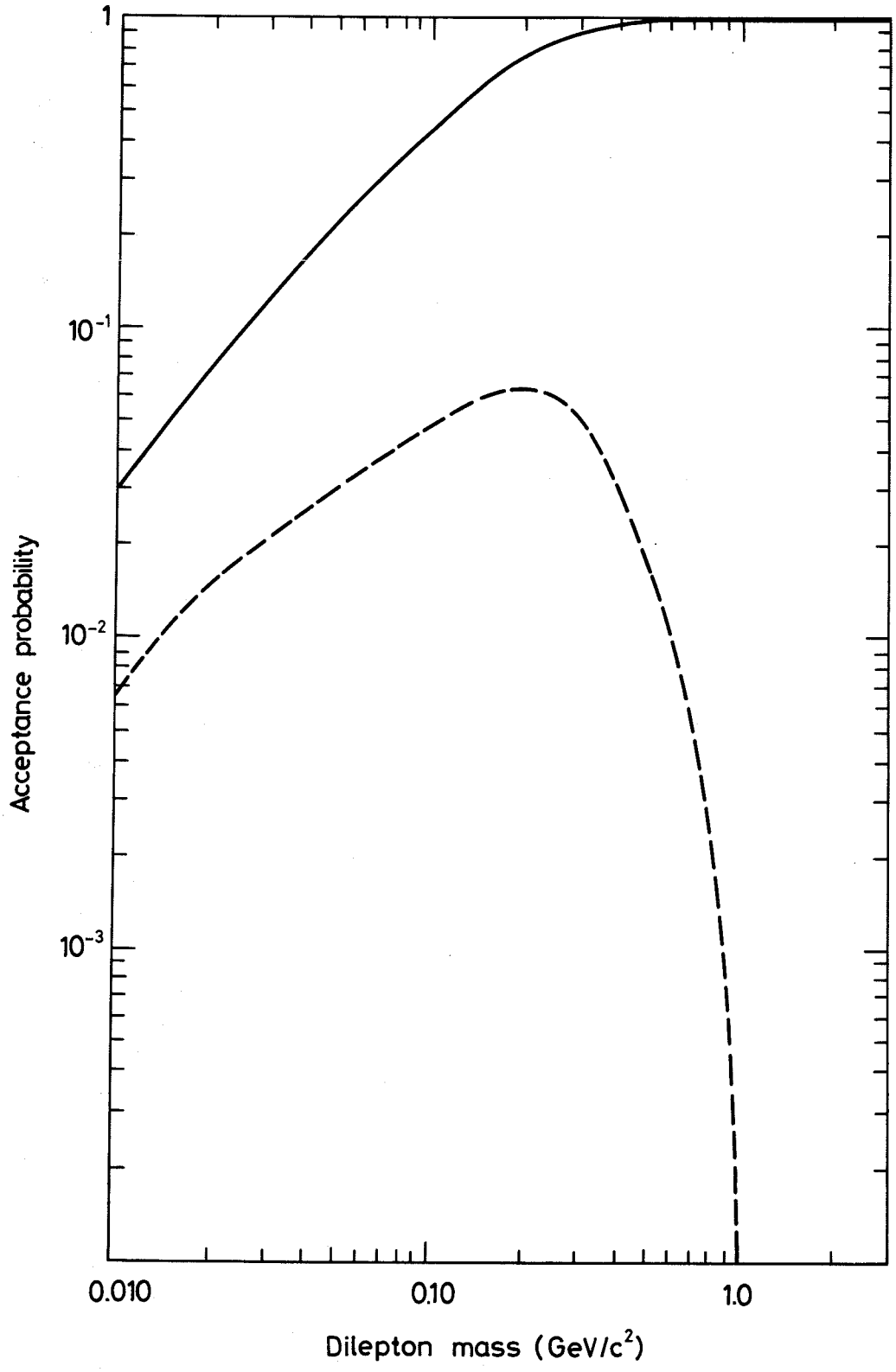
1
10^{-1}
10^{-2}
10^{-3}
Acceptance probability
0.010
0.10
1.0
Dilepton mass (GeV/c^2)

Fig. 14

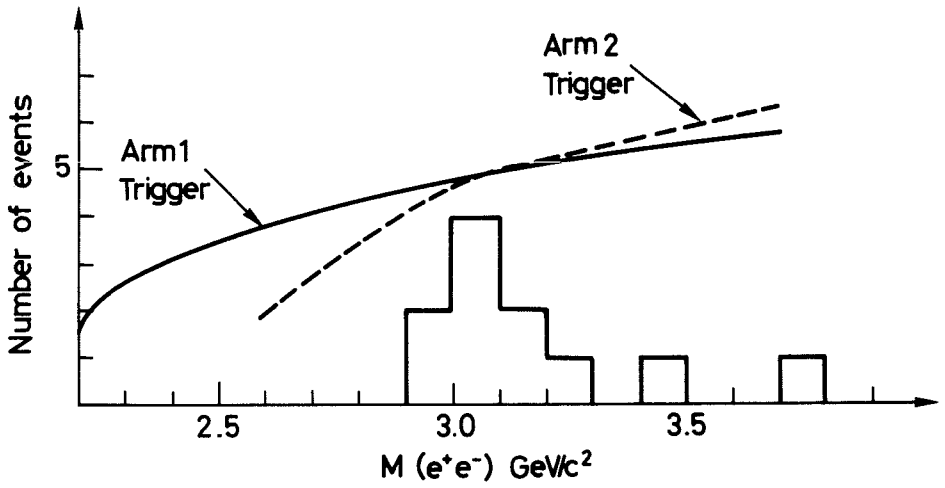
Arm 2
Trigger
Arm1
Trigger
Number of events
5
2.5
3.0
3.5
M (e⁺e⁻) GeV/c²

Fig. 15

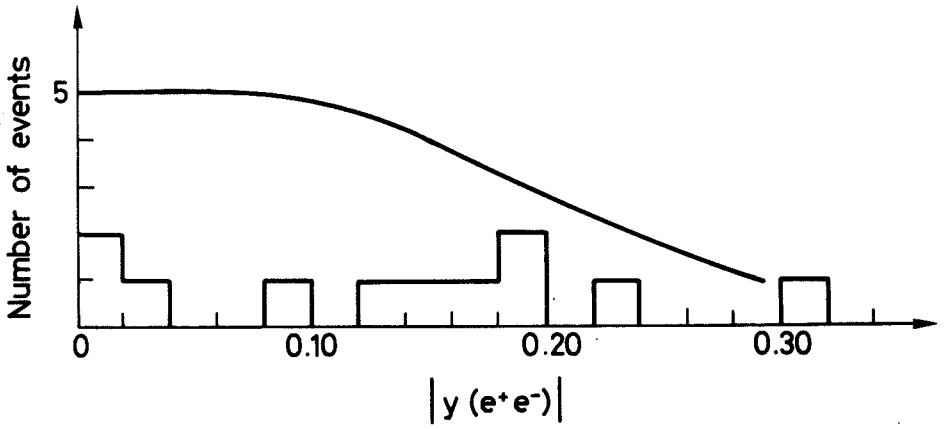
Number of events
5
0
0.10
0.20
0.30
|y (e⁺e⁻)|

Fig. 16

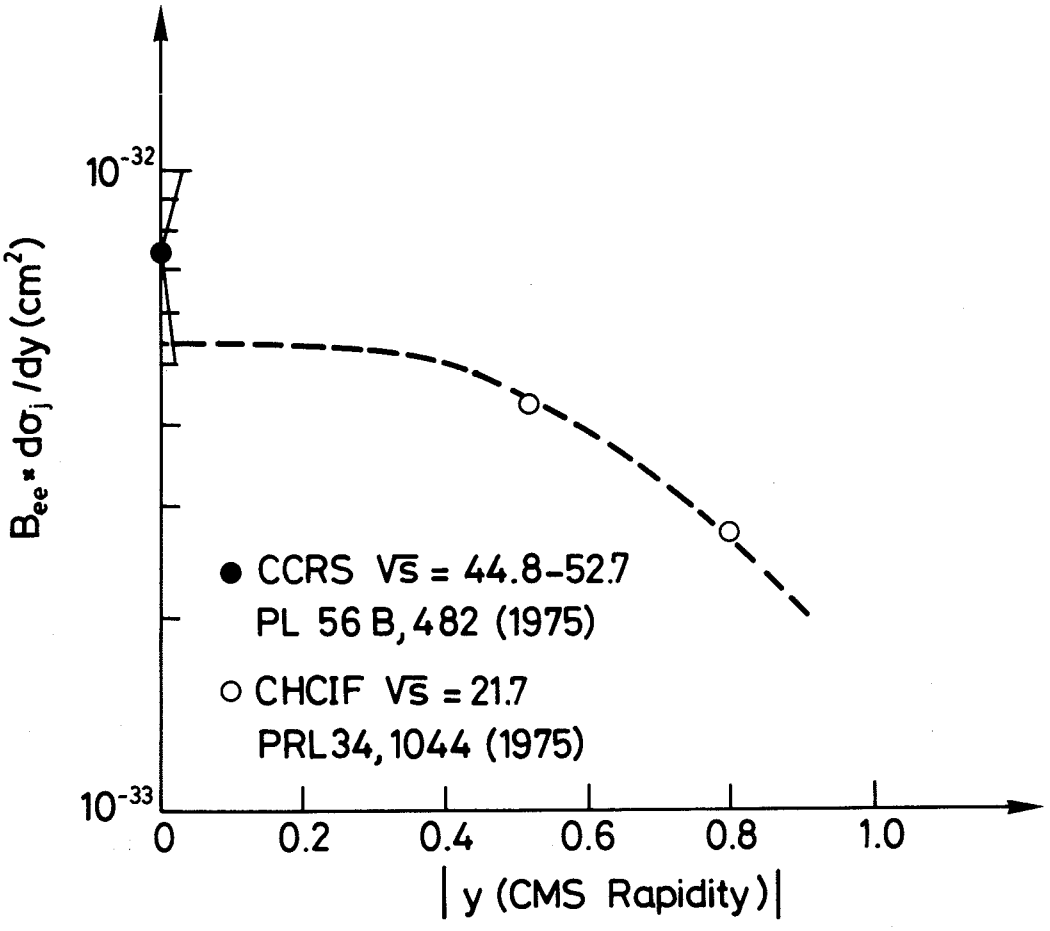
10^{-32}
10^{-33}
$B_{ee} * d\sigma_j / dy\ (cm^2)$
● CCRS $\sqrt{s}$ = 44.8-52.7
PL 56 B, 482 (1975)
○ CHCIF $\sqrt{s}$ = 21.7
PRL34, 1044 (1975)
0
0.2
0.4
0.6
0.8
1.0
| y (CMS Rapidity) |

Fig. 17

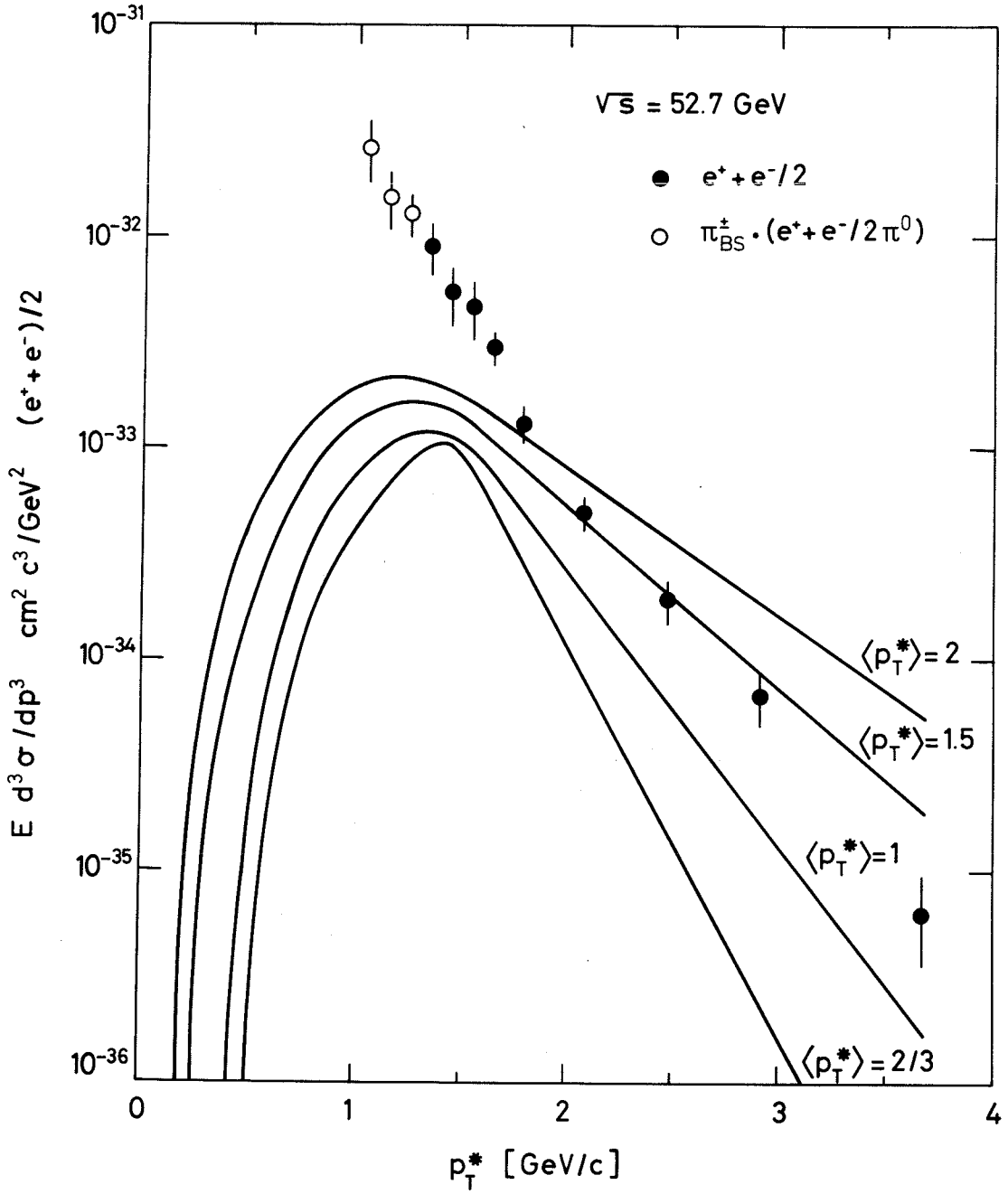
10^{-31}
10^{-32}
10^{-33}
10^{-34}
10^{-35}
10^{-36}
$\sqrt{s}$ = 52.7 GeV
$e^+ + e^-/2$
$\pi^{\pm}_{BS} \cdot (e^+ + e^-/2\pi^0)$
$\langle p_T^* \rangle = 2$
$\langle p_T^* \rangle = 1.5$
$\langle p_T^* \rangle = 1$
$\langle p_T^* \rangle = 2/3$
$E\, d^3\sigma/dp^3$ cm^2 c^3/GeV^2 $(e^+ + e^-)/2$
0
1
2
3
4
p_T^* [GeV/c]

Fig. 18

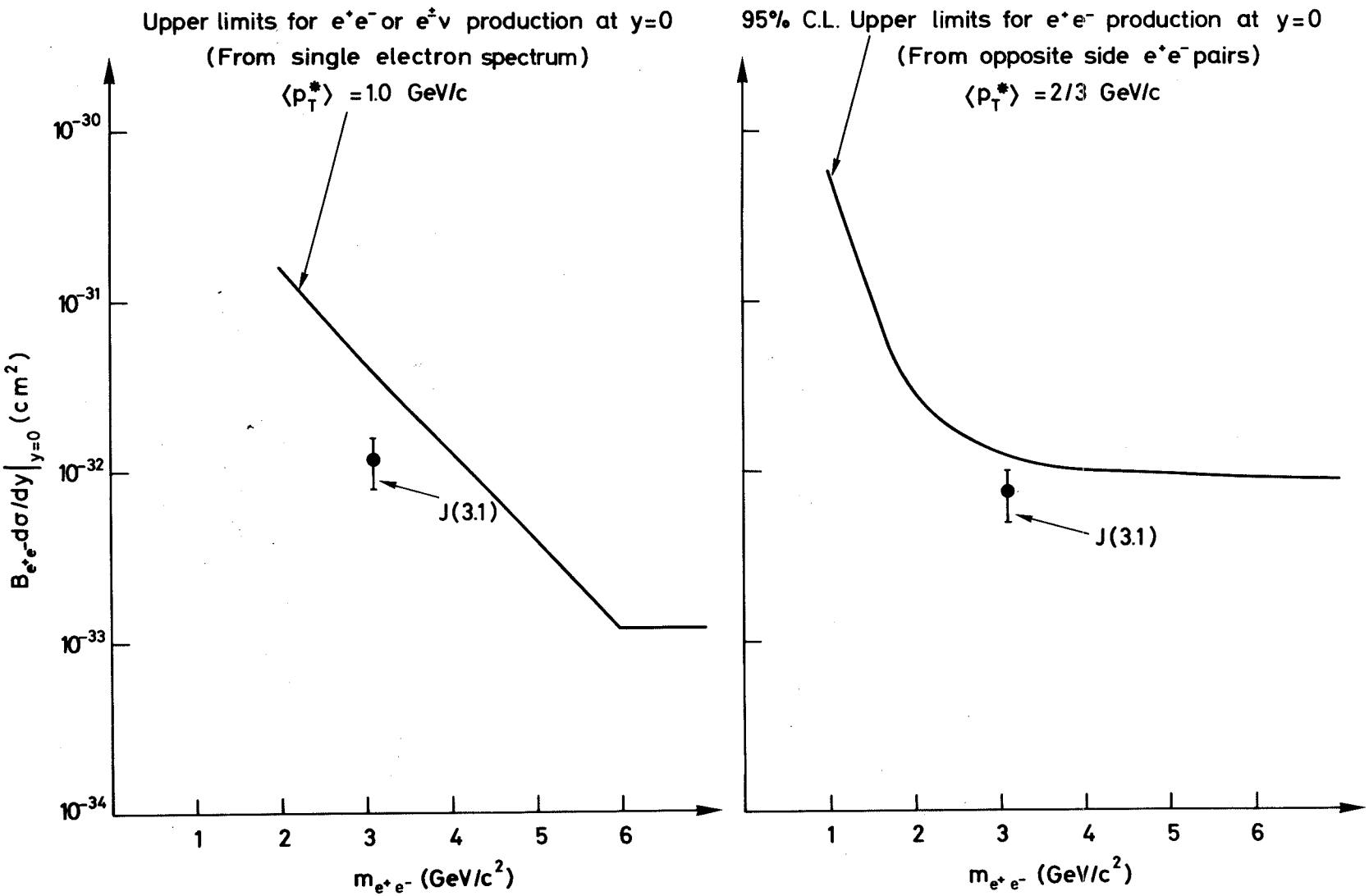
Upper limits for e⁺e⁻ or e±ν production at y=0
(From single electron spectrum)
⟨p*T⟩ =1.0 GeV/c
95% C.L. Upper limits for e⁺e⁻ production at y=0
(From opposite side e⁺e⁻ pairs)
⟨p*T⟩ =2/3 GeV/c
B e⁺e⁻ dσ/dy|y=0 (cm²)
10⁻³⁰
10⁻³¹
10⁻³²
10⁻³³
10⁻³⁴
J(3.1)
J(3.1)
1
2
3
4
5
6
m e⁺e⁻ (GeV/c²)
m e⁺e⁻ (GeV/c²)

Fig. 19

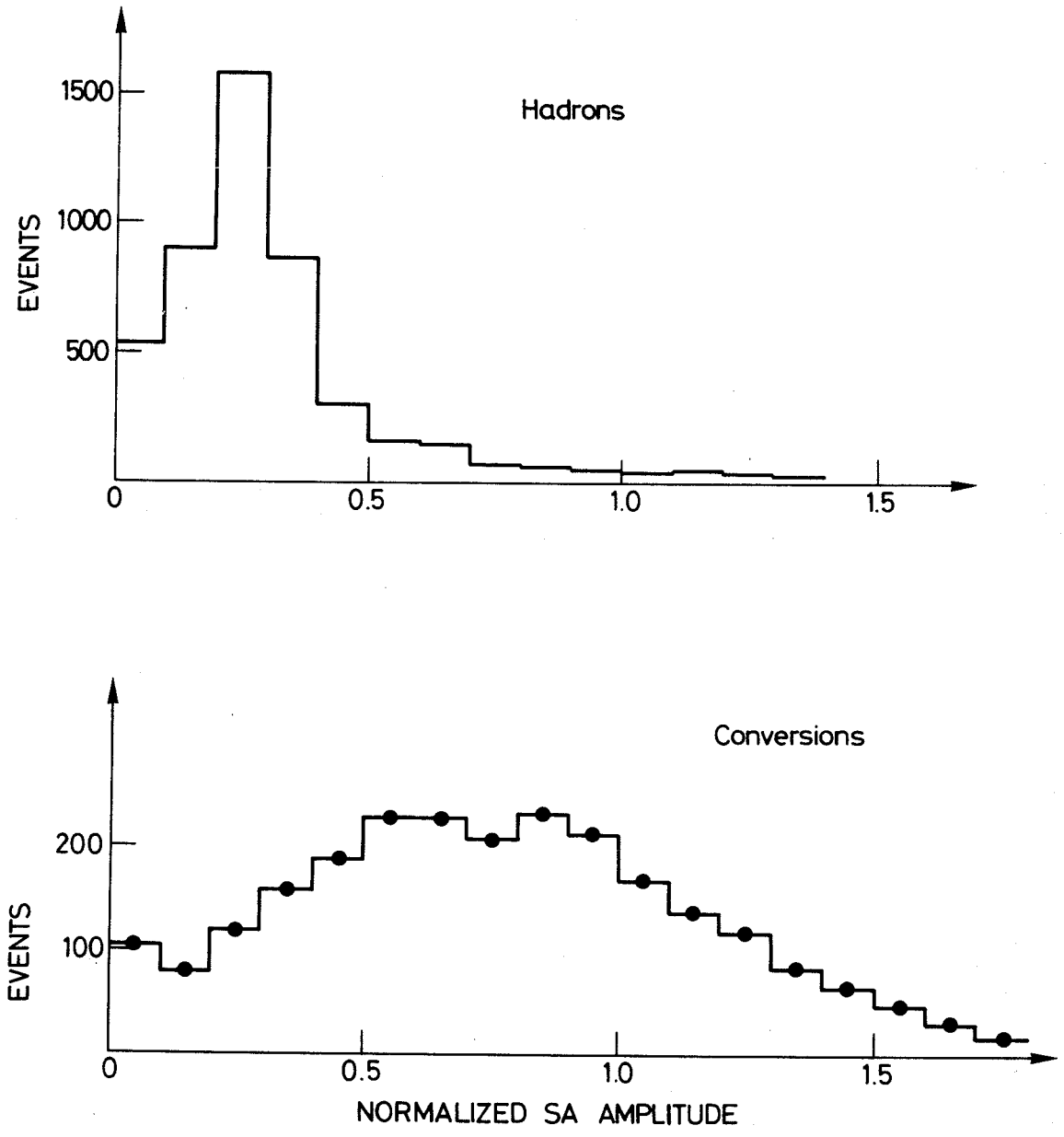
Hadrons
EVENTS
1500
1000
500
0
0.5
1.0
1.5
Conversions
EVENTS
200
100
0
0.5
1.0
1.5
NORMALIZED SA AMPLITUDE

Fig. 20

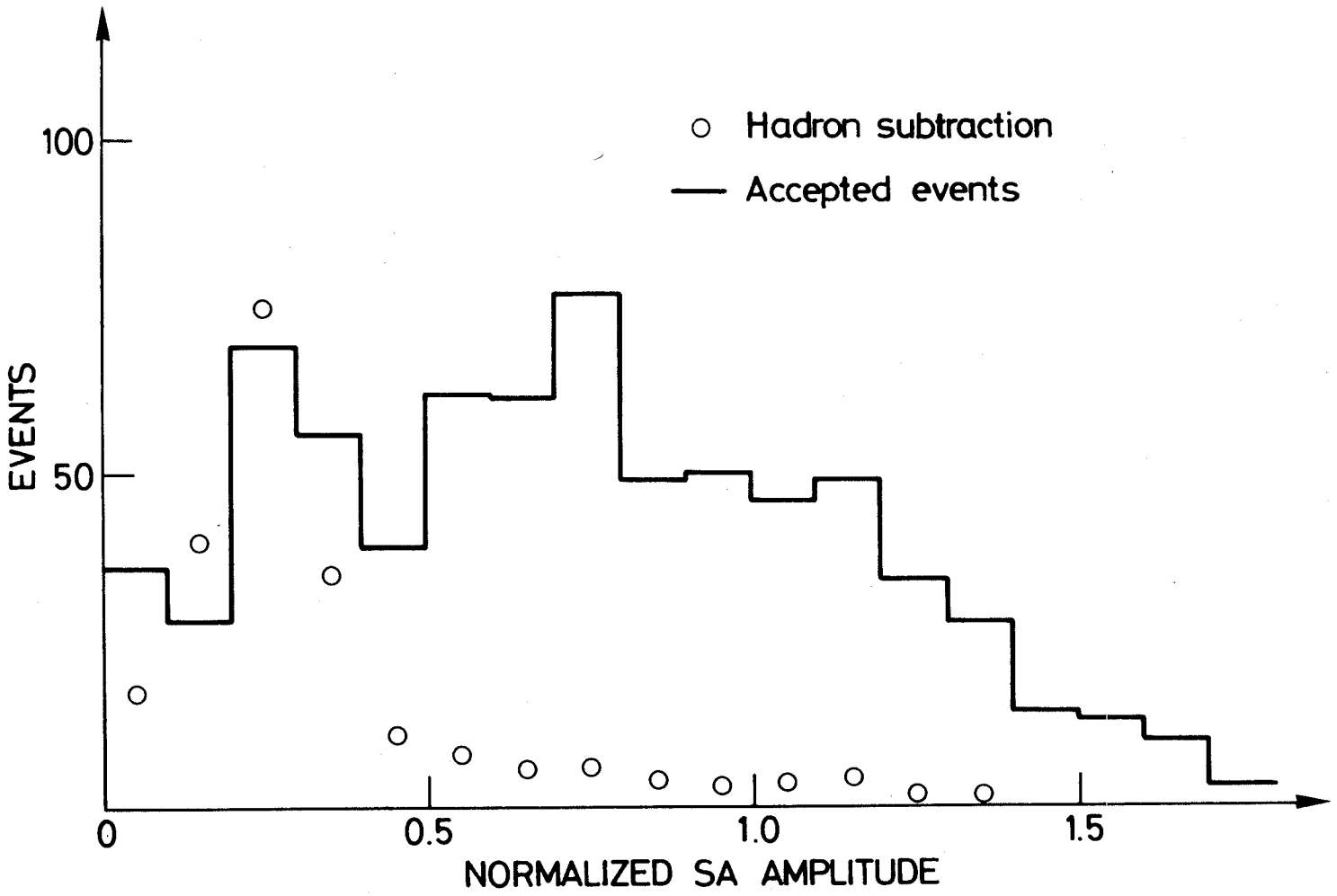
Hadron subtraction
Accepted events
100
50
EVENTS
0
0.5
1.0
1.5
NORMALIZED SA AMPLITUDE

Fig. 21

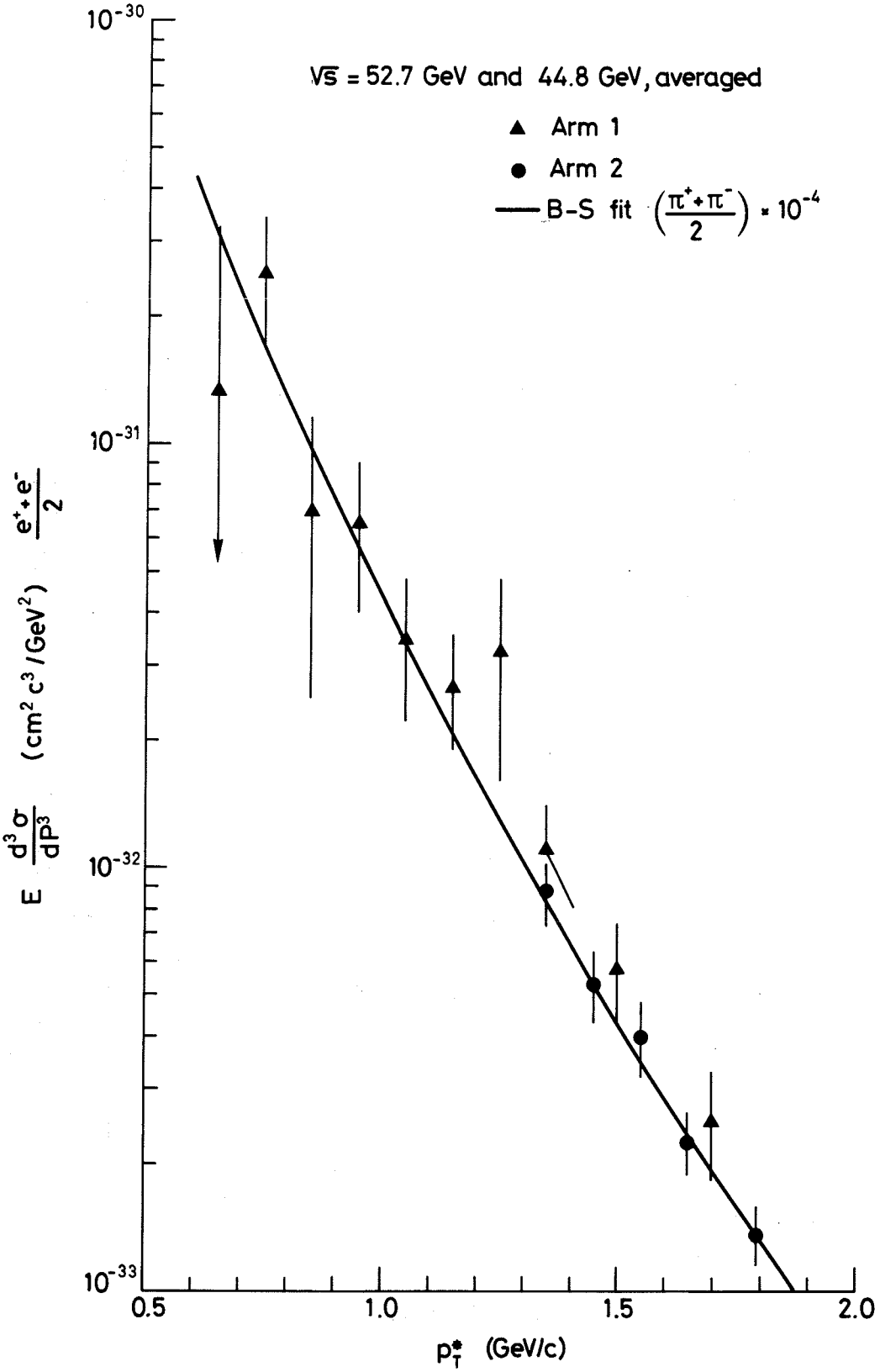
10^{-30}
10^{-31}
10^{-32}
10^{-33}
$\sqrt{s}$ = 52.7 GeV and 44.8 GeV, averaged
Arm 1
Arm 2
B-S fit $\left(\frac{\pi^+ + \pi^-}{2}\right) \times 10^{-4}$
$E \frac{d^3\sigma}{dP^3}$ $(cm^2 c^3/GeV^2)$ $\frac{e^+ + e^-}{2}$
0.5
1.0
1.5
2.0
p_T^* (GeV/c)

Fig. 22

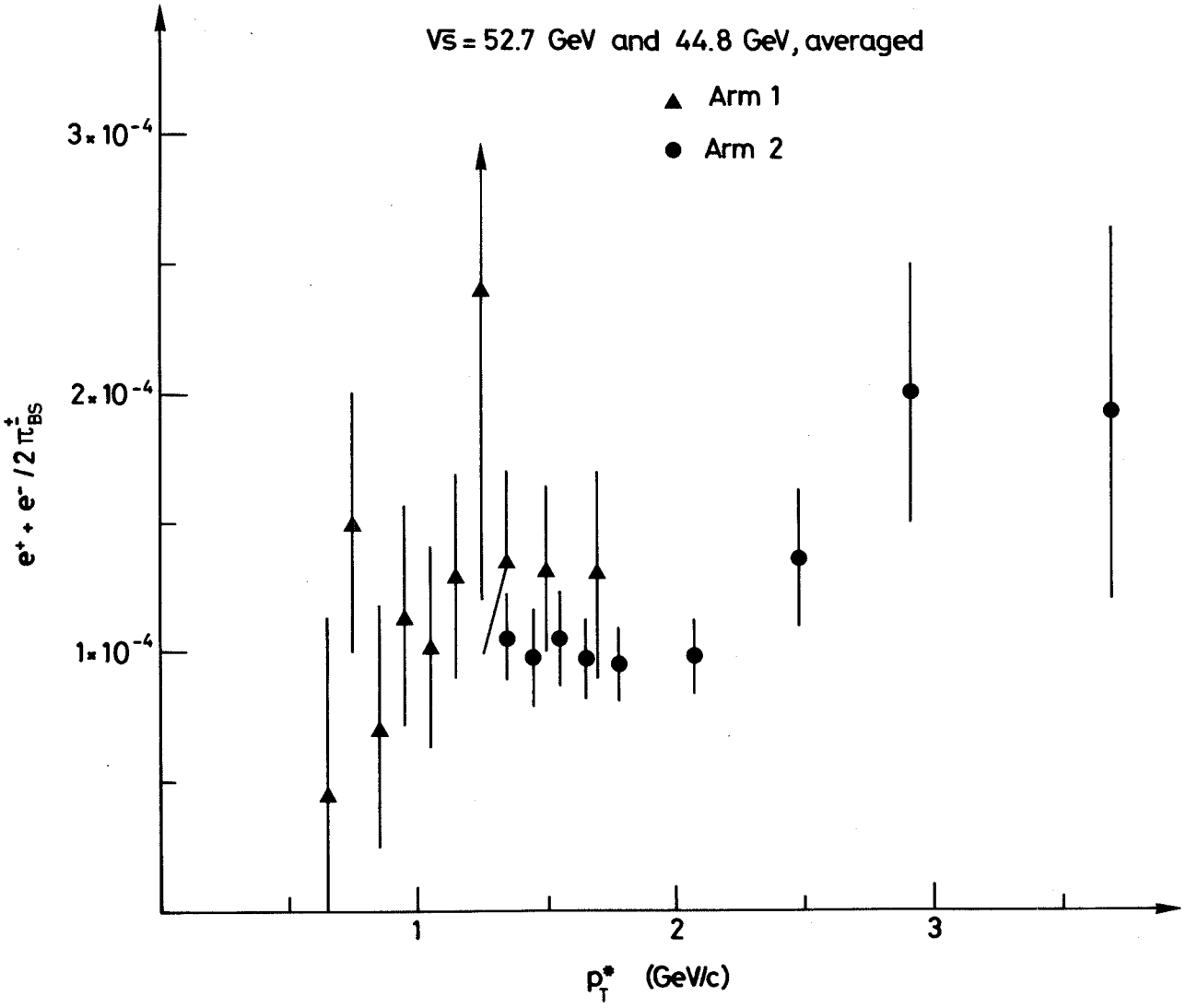
√s = 52.7 GeV and 44.8 GeV, averaged
Arm 1
Arm 2
3 × 10⁻⁴
2 × 10⁻⁴
1 × 10⁻⁴
e⁺ + e⁻ / 2 π±BS
1
2
3
p*T (GeV/c)

Fig. 23